

Global Robustness Evaluation of Deep Neural Networks with Provable Guarantees for the L_0 Norm

Wenjie Ruan¹, Min Wu¹, Youcheng Sun¹, Xiaowei Huang²
Daniel Kroening¹, and Marta Kwiatkowska¹

¹University of Oxford, UK

{wenjie.ruan; min.wu; youcheng.sun}@cs.ox.ac.uk

{kroening; marta.kwiatkowska}@cs.ox.ac.uk

²University of Liverpool, UK

xiaowei.huang@liverpool.ac.uk

Abstract. Deployment of deep neural networks (DNNs) in safety- or security-critical systems requires provable guarantees on their correct behaviour. A common requirement is robustness to adversarial perturbations in a neighbourhood around an input. In this paper we focus on the L_0 norm and aim to compute, for a trained DNN and an input, the maximal radius of a safe norm ball around the input within which there are no adversarial examples. Then we define global robustness as an expectation of the maximal safe radius over a test data set. We first show that the problem is NP-hard, and then propose an approximate approach to iteratively compute lower and upper bounds on the network’s robustness. The approach is *anytime*, i.e., it returns intermediate bounds and robustness estimates that are gradually, but strictly, improved as the computation proceeds; *tensor-based*, i.e., the computation is conducted over a set of inputs simultaneously, instead of one by one, to enable efficient GPU computation; and has *provable guarantees*, i.e., both the bounds and the robustness estimates can converge to their optimal values. Finally, we demonstrate the utility of the proposed approach in practice to compute tight bounds by applying and adapting the anytime algorithm to a set of challenging problems, including global robustness evaluation, competitive L_0 attacks, test case generation for DNNs, and local robustness evaluation on large-scale ImageNet DNNs. We release the code of all case studies via GitHub¹.

1 Introduction

Deep neural networks (DNNs) have achieved significant breakthroughs in the past few years and are now being deployed in many applications. However, in safety-critical domains, where human lives are at stake, and security-critical applications, which often have significant financial risks, concerns have been raised about the reliability of this technique. In established industries, e.g., avionics and automotive, such concerns have to be addressed during the certification process before the deployment of the product. During the certification process, the manufacturer needs to demonstrate to the relevant certification authority, e.g., the European Aviation Safety Agency or the Vehicle Certification Agency, that the product behaves correctly with respect to a set of high-level requirements. For this purpose, it is necessary to develop techniques for discovering critical requirements and supporting the case that these requirements are met by the product.

¹ The code is available in <https://github.com/TrustAI/L0-TRE>

Safety certification for DNNs is challenging owing to the black-box nature of DNNs and the lack of rigorous foundations. An important low-level requirement for DNNs is the robustness to input perturbations. DNNs have been shown to suffer from poor robustness because of their susceptibility to *adversarial examples* [29]. These are small modifications to an input, sometimes imperceptible to humans, that make the network unstable. As a result, significant effort has been directed towards approaches for crafting adversarial examples or defending against them [2, 5, 18]. However, the cited approaches provide *no* formal guarantees, i.e., no conclusion can be made whether adversarial examples remain or how close crafted adversarial examples are to the optimal ones.

Recent efforts in the area of automated verification [8,9] have instead focused on methods that generate adversarial examples, if they exist, and provide rigorous robustness proofs otherwise. These techniques rely on either a layer-by-layer exhaustive search of the neighbourhood of an image [8], or a reduction to a constraint solving problem by encoding the network as a set of constraints [9]. Constraint-based approaches are limited to small networks. Exhaustive search, on the other hand, applies to large networks but suffers from the state-space explosion problem. To mitigate this, a Monte-Carlo tree search has been employed [31]. Moreover, a game-based approximate verification approach that can provide provable guarantees has been proposed [32].

This paper proposes a novel approach to quantify the robustness of DNNs that offers a balance between the guaranteed accuracy of the method (thus, a feature so far exclusive to formal approaches) and the efficiency of algorithms that search for adversarial examples (without providing any guarantees). We consider the *global* robustness problem, which is a generalisation of the local, pointwise robustness problem. Specifically, we define a maximum safe radius for every input and then evaluate robustness over a given test dataset, i.e., a finite set of inputs. Global robustness is defined as the expected maximum safe radius over the test examples. We focus on the L_0 norm, which measures the distance between two matrices (e.g., two input images) by counting the number of elements (e.g., pixels) that are different.

The key idea of our approach is to generate sequences of lower and upper bounds for global robustness. Our method is *anytime*, *tensor-based*, and offers *provable guarantees*. First, the method is *anytime* in the sense that it can return intermediate results, including upper and lower bounds and robustness estimates. We prove that our approach can gradually, but strictly, improve these bounds and estimates as the computation proceeds. Second, it is *tensor-based*. As we are working with a set of inputs, a straightforward approach is to perform robustness evaluation for the inputs individually and to then merge the results. However, this is inefficient, as the set of inputs is large. To exploit the parallelism offered by GPUs, our approach uses tensors. A tensor is a finite set of multi-dimensional arrays, and each element of the set represents one input. A good tensor-based algorithm uses tensor operations whenever possible. Third, our approach offers *provable guarantees*. We show that the intermediate bounds and the robustness estimates will converge to their optimal values in finite time, although this may be impractical for large networks.

We implement our approach in a tool we name L0-TRE (“Tensor-based Robustness Evaluation for the L_0 Norm”), and conduct experiments on a set of challenging problems, including *Case Study 1*: global robustness evaluation; *Case Study 2*: competitive L_0 attacks; *Case Study 3*: test case generation; *Case Study 4*: guidance for the design of robust DNN architectures; and *Case Study 5*: saliency map generation for model interpretability

and local robustness evaluation on five ImageNet DNNs including AlexNet, VGG-16/19 and ResNet-50/101.

All applications above require only simple adaptations of our method, e.g., slight modifications of the constraints or objective functions, or the addition of extra constraints. This demonstrates that our new technique is flexible enough to deliver a wide range of promising applications. The main contributions of this paper are as follows:

- We propose a novel method to quantify global robustness of DNNs w.r.t. the L_0 -norm. This offers two key advantages, including *i*) theoretical lower and upper bounds to guarantee its convergence; and *ii*) explicit tensor-based parallelisation on GPUs with high computational efficiency.
- With simple adaptations, we show the utility of the proposed method on a broad range of applications, including *i*) anytime global robustness evaluation; *ii*) competitive L_0 adversarial attacks; and *iii*) test case generation, etc.
- We perform a rigorous theoretical analysis and extensive empirical case studies to support the claims above. We test our tool on 15 different deep neural networks, including eight MNIST DNNs, two CIFAR-10 DNNs and five ImageNet DNNs.

2 Problem Formulation

Let $f : \mathbb{R}^n \rightarrow \mathbb{R}^m$ be an N -layer neural network such that, for a given input $x \in \mathbb{R}^n$, $f(x) = (c_1(x), c_2(x), \dots, c_m(x)) \in \mathbb{R}^m$ represents the confidence values for m classification labels. Specifically, we have

$$f(x) = f_N(f_{N-1}(\dots f_1(x; W_1, b_1); W_2, b_2); \dots); W_N, b_N) \quad (1)$$

where W_i and b_i for $i = 1, 2, \dots, N$ are learnable parameters, and $f_i(z_{i-1}; W_{i-1}, b_{i-1})$ is the function that maps the output of layer $i-1$, i.e., z_{i-1} , to the input of layer i . Without loss of generality, we normalise the input to $x \in [0, 1]^n$. The output $f(x)$ is usually normalised to be in $[0, 1]^m$ with a softmax layer. We denote the classification label of input x by $cl(f, x) = \arg \max_{j=1, \dots, m} c_j(x)$. Note that both f and cl can be generalised to work with a set T_0 of inputs, i.e., $f(T_0)$ and $cl(f, T_0)$, in the standard way.

Definition 1 (Safe Norm Ball) *Given a network $f : \mathbb{R}^n \rightarrow \mathbb{R}^m$, an input $x_0 \in \mathbb{R}^n$, a distance metric $\|\cdot\|_D$ and a real number $d \in \mathbb{R}$, a norm ball $B(f, x_0, \|\cdot\|_D, d)$ is a subspace of \mathbb{R}^n such that*

$$B(f, x_0, \|\cdot\|_D, d) = \{x \mid \|x_0 - x\|_D \leq d\}. \quad (2)$$

The number d is called the radius of $B(f, x_0, \|\cdot\|_D, d)$. A norm ball $B(f, x_0, \|\cdot\|_D, d)$ is safe if for all $x \in B(f, x_0, \|\cdot\|_D, d)$ we have $cl(f, x) = cl(f, x_0)$.

Intuitively, a norm ball $B(f, x_0, \|\cdot\|_D, d)$ includes all inputs whose distance to x_0 , measured by a metric $\|\cdot\|_D$, is within d .

Definition 2 (Maximum Radius of a Safe Norm Ball) *Let d be the radius of a safe norm ball $B(f, x_0, \|\cdot\|_D, d)$. If for all $d' > d$ we have that $B(f, x_0, \|\cdot\|_D, d')$ is not safe, then d is called the maximum safe radius, denoted by $d_m(f, x_0, \|\cdot\|_D)$. Formally,*

$$d_m(f, x_0, \|\cdot\|_D) = \arg \sup_d \{B(f, x_0, \|\cdot\|_D, d) \text{ is safe} \mid d \in \mathbb{R}, d > 0\}. \quad (3)$$

We define the (*global*) robustness evaluation problem over a testing dataset T , which is a set of i.i.d. inputs sampled from a distribution μ representing the problem f is working on. We use $|T|$ to denote the number of inputs in T . When $|T| = 1$, we call it *local* robustness.

Definition 3 (Robustness Evaluation) *Given a network f , a finite set T_0 of inputs, and a distance metric $\|\cdot\|_D$, the robustness evaluation, denoted as $R(f, T_0, \|\cdot\|_D)$, is an optimization problem:*

$$\begin{aligned} & \min_T \|T_0 - T\|_D \\ \text{s.t.} \quad & cl(f, x_i) \neq cl(f, x_{0,i}) \quad \text{for } i = 1, \dots, |T_0| \end{aligned} \quad (4)$$

where $T = (x_i)_{i=1 \dots |T_0|}$, $T_0 = (x_{0,i})_{i=1 \dots |T_0|}$, and $x_i, x_{0,i} \in [0, 1]^n$.

Intuitively, we aim to find a minimum distance between the original set T_0 and a new, homogeneous set T of inputs such that all inputs in T_0 are misclassified. The two sets T_0 and T are homogeneous if they have the same number of elements and their corresponding elements are of the same type.

L_0 Norm The distance metric $\|\cdot\|_D$ can be any mapping $\|\cdot\|_D : \mathbb{R}^n \times \mathbb{R}^n \rightarrow [0, \infty]$ that satisfies the metric conditions. In this paper, we focus on the L_0 metric. For two inputs x_0 and x , their L_0 distance, denoted as $\|x - x_0\|_0$, is the number of elements that are different. When working with test datasets, we define

$$\begin{aligned} \|T - T_0\|_0 &= \mathbb{E}_{x_0 \in T_0} [\|x - x_0\|_0] \quad (\text{our definition}) \\ &= \frac{1}{|T_0|} \sum_{x_0 \in T_0} \|x - x_0\|_0 \quad (\text{all inputs in } T_0 \text{ are i.i.d.}) \end{aligned} \quad (5)$$

where $x \in T$ is a homogeneous input of $x_0 \in T_0$. While other norms such as L_1 , L_2 and L_∞ have been widely applied for generating adversarial examples [11, 18], studies based on the L_0 norm are few and far between. In the Appendix, we justify why L_0 is the appropriate metric for our goals.

3 Anytime Robustness Evaluation

The accurate evaluation of robustness in Definition 3 is hard in terms of L_0 -norm distance. In Appendix A.1, we give the computational complexity and prove its NP-hardness.

In this paper, we propose to compute lower and upper bounds, and then gradually, but *strictly*, improve the bounds so that the gap between them can eventually be closed in finite time. Although the realistic running time can be long, this *anytime* approach provides pragmatic means to track progress. Experimental results in Section 5 show that our approach is able to achieve *tight* bounds *efficiently* in practice.

Definition 4 (Sequences of Bounds) *Given a robustness evaluation problem $R(f, T_0, \|\cdot\|_D)$, a sequence $\mathcal{L}(T_0) = \{l_1, l_2, \dots, l_k\} \in \mathbb{R}$ is an incremental lower bound sequence if, for all $1 \leq i < j \leq k$, we have $l_i \leq l_j \leq R(f, T_0, \|\cdot\|_D)$. The sequence is strict, denoted as $\mathcal{L}_s(T_0)$, if for all $1 \leq i < j \leq k$, we have either $l_i < l_j$ or $l_i = l_j = R(f, T_0, \|\cdot\|_D)$. Similarly, we can define a decremental upper bound sequence $\mathcal{U}(T_0)$ and a strict decremental upper bound sequence $\mathcal{U}_s(T_0)$.*

We will, in Section 4, introduce our algorithms on computing these two sequences of lower and upper bounds. For now, assume they exist, then at a certain time $t > 0$, $l_t \leq R(f, \mathbb{T}_0, \|\cdot\|_D) \leq u_t$ holds.

Definition 5 (Anytime Robustness Evaluation) For a given range $[l_t, u_t]$, we define its centre and radius as follows.

$$U_c(l_t, u_t) = \frac{1}{2}(l_t + u_t) \quad \text{and} \quad U_r(l_t, u_t) = \frac{1}{2}(u_t - l_t). \quad (6)$$

The anytime evaluation of $R(f, \mathbb{T}_0, \|\cdot\|_D)$ at time t , denoted as $R_t(f, \mathbb{T}_0, \|\cdot\|_D)$, is the pair $(U_c(l_t, u_t), U_r(l_t, u_t))$.

The anytime evaluation will be returned whenever the computational procedure is interrupted. Intuitively, we use $U_c(l_t, u_t)$ to represent the current estimation, and $U_r(l_t, u_t)$ to represent its error bound. Essentially, we can bound the true robustness $R(f, \mathbb{T}_0, \|\cdot\|_D)$ via the anytime robustness evaluation. Let f be a network and $\|\cdot\|_D$ a distance metric. At any time $t > 0$, the anytime evaluation $R_t(f, \mathbb{T}_0, \|\cdot\|_D) = (U_c(l_t, u_t), U_r(l_t, u_t))$ such that

$$U_c(l_t, u_t) - U_r(l_t, u_t) \leq R(f, \mathbb{T}_0, \|\cdot\|_D) \leq U_c(l_t, u_t) + U_r(l_t, u_t). \quad (7)$$

4 Tensor-based Algorithms for Upper and Lower Bounds

We present our approach to generate the sequences of bounds.

Definition 6 (Complete Set of Subspaces for an Input) Given an input $x_0 \in [0, 1]^n$ and a set of t dimensions $T \subseteq \{1, \dots, n\}$ such that $|T| = t$, the subspace for x_0 , denoted by $X_{x_0, T}$, is a set of inputs $x \in [0, 1]^n$ such that $x(i) \in [0, 1]$ for $i \in T$ and $x(i) = x_0(i)$ for $i \in \{1, \dots, n\} \setminus T$. Furthermore, given an input $x_0 \in [0, 1]^n$ and a number $t \leq n$, we define

$$\mathcal{X}(x_0, t) = \{X_{x_0, T} \mid T \subseteq \{1, \dots, n\}, |T| = t\} \quad (8)$$

as the complete set of subspaces for input x_0 .

Intuitively, elements in $X_{x_0, T}$ share the same value with x_0 on the dimensions other than T , and may take any legal value for the dimensions in T . Moreover, $\mathcal{X}(x_0, t)$ includes all sets $X_{x_0, T}$ for any possible combination T with t dimensions.

Next, we define the subspace sensitivity for a subspace w.r.t. a network f , an input x_0 and a test dataset \mathbb{T}_0 . Recall that $f(x) = (c_1(x), c_2(x), \dots, c_m(x))$.

Definition 7 (Subspace Sensitivity) Given an input subspace $X \subseteq [0, 1]^n$, an input $x_0 \in [0, 1]^n$ and a label j , the subspace sensitivity w.r.t. X , x_0 , and j is defined as

$$S(X, x_0, j) = c_j(x_0) - \inf_{x \in X} c_j(x). \quad (9)$$

Let t be an integer. We define the subspace sensitivity for \mathbb{T}_0 and t as

$$S(\mathbb{T}_0, t) = (S(X_{x_0}, x_0, j_{x_0}))_{X_{x_0} \in \mathcal{X}(x_0, t), x_0 \in \mathbb{T}_0} \quad (10)$$

where $j_{x_0} = \arg \max_{i \in \{1, \dots, m\}} c_i(x_0)$ is the classification label of x_0 by network f .

Intuitively, $S(X, x_0, j)$ is the maximal decrease of confidence value of the output label j that can be witnessed from the set X , and $S(\mathbb{T}_0, t)$ is the two-dimensional array of the maximal decreases of confidence values of the classification labels for all subspaces in $\mathcal{X}(x_0, t)$ and all inputs in \mathbb{T}_0 . It is not hard to see that $S(X, x_0, j) \geq 0$.

Given a test dataset \mathbb{T}_0 and an integer $t > 0$, the number of elements in $S(\mathbb{T}_0, t)$ is in $O(|\mathbb{T}_0| \cdot n^t)$, i.e., polynomial in $|\mathbb{T}_0|$ and exponential in t . Note that, by Equation (9), every element in $S(\mathbb{T}_0, t)$ represents an optimisation problem. E.g., for \mathbb{T}_0 , a set of 20 MNIST images, and $t = 1$, this would be $28 \times 28 \times 20 = 15,680$ one-dimensional optimisation problems. In the next section, we give a tensor-based formulation and an algorithm to solve this challenging problem via GPU parallelisation.

4.1 Tensor-based Parallelisation for Computing Subspace Sensitivity

A tensor $\mathcal{T} \in \mathbb{R}^{I_1 \times I_2 \times \dots \times I_N}$ in an N -dimensional space is a mathematical object that has $\prod_{m=1}^N I_m$ components and obeys certain transformation rules. Intuitively, tensors are generalisations of vectors (i.e., one index) and matrices (i.e., two indices) to an arbitrary number of indices. Many state-of-the-art deep learning libraries, such as Tensorflow and Keras, are utilising the tensor format to parallelise the computation with GPUs. However, it is nontrivial to write an algorithm working with tensors due to the limited set of operations on tensors.

The basic idea of our algorithm is to transform a set of nonlinear, nonconvex optimisation problems as given in Equation (10) into a tensor formulation, and solve a set of optimisation problems via a few DNN queries. First, we introduce the following operations on tensors we use in our algorithm.

Definition 8 (Mode- n Unfolding and Folding) *Given a tensor $\mathcal{T} \in \mathbb{R}^{I_1 \times I_2 \times \dots \times I_N}$, the mode- n unfolding of \mathcal{T} is a matrix $\mathbf{U}_{[n]}(\mathcal{T}) \in \mathbb{R}^{I_n \times I_M}$ such that $M = \prod_{k=1, k \neq n}^N I_k$ and $\mathbf{U}_{[n]}(\mathcal{T})$ is defined by the mapping from element (i_1, i_2, \dots, i_N) to (i_n, j) , with*

$$j = \sum_{k=1, k \neq n}^N i_k \times \prod_{m=k+1, m \neq n}^N I_m.$$

Accordingly, the tensor folding \mathbf{F} folds an unfolded tensor back from a matrix to a full tensor. Tensor unfolding and folding are dual operations and link tensors and matrices.

Given a neural network f , a number t and a test dataset \mathbb{T}_0 , each $x_i \in \mathbb{T}_0$ generates a complete set $\mathcal{X}(x_i, t)$ of subspaces. Let $|\mathbb{T}_0| = p$ and $|\mathcal{X}(x_i, t)| = k$. Note that for different x_i and x_j , we have $|\mathcal{X}(x_i, t)| = |\mathcal{X}(x_j, t)|$. Given an error tolerance $\epsilon > 0$, by applying grid search, we can recursively sample $\Delta = 1/\epsilon$ numbers in each dimension, and turn each subspace $X_{x_i} \in \mathcal{X}(x_i, t)$ into a two-dimensional grid $\mathcal{G}(X_{x_i}) \in \mathbb{R}^{n \times \Delta^t}$. We can formulate the following tensor:

$$\mathcal{T}(\mathbb{T}_0, t) = \text{Tensor}((\mathcal{G}(X_{x_i}))_{x_i \in \mathbb{T}_0, X_{x_i} \in \mathcal{X}(x_i, t)}) \in \mathbb{R}^{n \times \Delta^t \times p \times k} \quad (11)$$

In Sec. 4.3, we show that grid search provides the guarantee of reaching the global minimum by utilizing the Lipschitz continuity in DNNs.

Then, we apply the mode-1 tensor unfolding operation to have $\mathbf{T}_{[1]}(\mathcal{T}(\mathbf{T}_0, t)) \in \mathbb{R}^{n \times M}$ such that $M = \Delta^t \cdot p \cdot k$. Then this tensor can be fed into the DNN f to obtain

$$Y(\mathbf{T}_0, t) = f(\mathbf{T}_{[1]}(\mathcal{T}(\mathbf{T}_0, t))) \in \mathbb{R}^M. \quad (12)$$

After computing $Y(\mathbf{T}_0, t)$, we apply a tensor folding operation to obtain

$$\mathcal{Y}(\mathbf{T}_0, t) = \mathbf{F}(Y(\mathbf{T}_0, t)) \in \mathbb{R}^{\Delta^t \times p \times k}. \quad (13)$$

Here, we should note the difference between $\mathbb{R}^{\Delta^t \cdot p \cdot k}$ and $\mathbb{R}^{\Delta^t \times p \times k}$, with the former being a one-dimensional array and the latter a tensor. On $\mathcal{Y}(\mathbf{T}_0, t)$, we search the minimum values along the first dimension to obtain²

$$V(\mathbf{T}_0, t)_{\min} = \min(\mathcal{Y}(\mathbf{T}_0, t), 1) \in \mathbb{R}^{p \times k} \quad (14)$$

Thus, we have now solved all $p \times k$ optimisation problems. We then construct the tensor

$$V(\mathbf{T}_0, t) = \overbrace{(c_{j_{x_i}}(x_i), \dots, c_{j_{x_i}}(x_i))}_{k}_{x_i \in \mathbf{T}_0} \in \mathbb{R}^{p \times k} \quad (15)$$

from the set \mathbf{T}_0 . Recall that $j_{x_i} = \arg \max_{k \in \{1, \dots, m\}} c_k(x_i)$. Intuitively, $V(\mathbf{T}_0, t)$ is the tensor that contains the starting points of the optimisation problems and $V(\mathbf{T}_0, t)_{\min}$ the resulting optimal values. The following theorem shows the correctness of our computation, where $S(\mathbf{T}_0, t)$ has been defined in Definition 7.

Theorem 1 *Let \mathbf{T}_0 be a test dataset and t an integer. We have $S(\mathbf{T}_0, t) = V(\mathbf{T}_0, t) - V(\mathbf{T}_0, t)_{\min}$.*

To perform the computation above, we only need a single DNN query in Equation (12).

4.2 Tensor-based Parallelisation for Computing Lower and Upper Bounds

Let $\mathcal{S}(\mathbf{T}_0, t) \in \mathbb{R}^{n \times p \times k}$ be the tensor obtained by replacing every element in $S(\mathbf{T}_0, t)$ with their corresponding inputs that, according to the computation of $V(\mathbf{T}_0, t)_{\min}$, cause the largest decreases on the confidence values of the classification labels. We call $\mathcal{S}(\mathbf{T}_0, t)$ the *solution tensor* of $S(\mathbf{T}_0, t)$. The computation of $\mathcal{S}(\mathbf{T}_0, t)$ can be done using very few tensor operations over $\mathcal{T}(\mathbf{T}_0, t)$ and $\mathcal{Y}(\mathbf{T}_0, t)$, which have been given in Section 4.1. We omit the details.

Lower Bounds We reorder $S(\mathbf{T}_0, t)$ and $\mathcal{S}(\mathbf{T}_0, t)$ w.r.t. the decreased values in $S(\mathbf{T}_0, t)$. Then, we retrieve the first row of the third dimension in tensor $\mathcal{S}(\mathbf{T}_0, t)$, i.e., $\mathcal{S}(\mathbf{T}_0, t)[:, :, 1] \in \mathbb{R}^{n \times p}$, and check whether $cl(f, \mathcal{S}(\mathbf{T}_0, t)[:, :, 1]) = cl(f, \mathbf{T}_0)$. The result is an array of Boolean values, each of which is associated with an input $x_i \in \mathbf{T}_0$. If any element associated with x_i in the resulting array is *false*, we conclude that $d_m(f, x_i, \|\cdot\|_D) = t - 1$, i.e., the maximum safe radius has been obtained and the computation for x_i has converged. On the other hand, if the element associated with x_i is *true*, we update the lower bound for x_i to t . After computing $\mathcal{S}(\mathbf{T}_0, t)$, no further DNN query is needed to compute the lower bounds.

² Here we use a Matlab notation $\min(Y, k)$, which computes the minimum values over the k -th dimension for a multi-dimensional array Y . Other notation to appear later is similar.

Upper Bounds The upper bounds are computed by iteratively applying perturbations based on the matrix $\mathcal{S}(\mathbf{T}_0, t)$ for every input in \mathbf{T}_0 until a misclassification occurs. However, doing this sequentially for all inputs would be inefficient, since we need to query the network f after every perturbation on each image.

We present an efficient tensor-based algorithm, which enables GPU parallelisation. The key idea is to construct a new tensor $\mathcal{N} \in \mathbb{R}^{n \times p \times k}$ to maintain all the accumulated perturbations over the original inputs \mathbf{T} .

- Initialisation: $\mathcal{N}[:, :, 1] = \mathcal{S}(\mathbf{T}_0, t)[[:, :, 1]$.
- Iteratively construct the i -th row until $i = k$:

$$\mathcal{N}[:, :, i] = \{\mathcal{N}[:, :, i-1] \boxminus \{\mathcal{N}[:, :, i-1] \cap \mathcal{S}(\mathbf{T}_0, t)[[:, :, i]\}\} \cup \{\mathcal{S}(\mathbf{T}_0, t)[[:, :, i] \boxminus \{\mathcal{N}[:, :, i-1] \cap \mathcal{S}(\mathbf{T}_0, t)[[:, :, i]\}\}\} \} \quad (16)$$

where \boxminus , \cap , and \cup are tensor operations: $\mathcal{N}_1 \boxminus \mathcal{N}_2$ removes the corresponding non-zero elements in \mathcal{N}_2 from \mathcal{N}_1 ; further, $\mathcal{N}_1 \cap \mathcal{N}_2$ retains those elements that have the same values and sets the other elements to 0; finally, $\mathcal{N}_1 \cup \mathcal{N}_2$ merges the non-zero elements from two tensors. The two operands of these operations are required to have the same type. Intuitively, $\mathcal{N}[:, :, i]$ represents the result of applying the first i perturbations recorded in $\mathcal{S}(\mathbf{T}_0, t)[[:, :, 1 : i]$.

Subsequently, we unfold \mathcal{N} and pass the result to the DNN f , which yields the classification labels $Y(\mathbf{U}_{[1]}(\mathcal{N})) \in \{1, \dots, m\}^{p \cdot k}$. After that, a tensor folding operation is applied to obtain $\mathcal{Y}(\mathbf{U}_{[1]}(\mathcal{N})) \in \{1, \dots, m\}^{p \times k}$. Finally, we can compute the minimum column index along each row such that misclassification happens, denoted by $\{m_1, m_2, \dots, m_p\}$ such that $1 \leq m_i \leq k$. Then we let

$$\mathbf{T} = \{\mathcal{N}_{:,i,m_i} \in \mathbb{R}^{n \times p} \mid x_i \in \mathbf{T}_0\}, \quad (17)$$

which is the optimal set of inputs as required in Definition 3.

After computing $\mathcal{S}(\mathbf{T}_0, t)$, we only need one further DNN query to obtain all upper bounds for a given test dataset \mathbf{T}_0 .

Tightening the Upper Bounds There may be redundancies in $\mathbf{T} - \mathbf{T}_0$, i.e., not all the changes in $\mathbf{T} - \mathbf{T}_0$ are necessary to observe misclassification. We therefore reduce the redundancies and thereby tighten the upper bounds. We reduce the tightening problem to an optimisation problem similar to that of Definition 3, which enables us to reuse the tensor-based algorithms given above.

Assume that $x_{0,i}$ and x_i are two corresponding inputs in \mathbf{T} and \mathbf{T}_0 , respectively, for $i \in \{1, \dots, |\mathbf{T}_0|\}$. By abuse of notation, we let $z_{0,i} = x_{0,i} - x_i$ be the part of $x_{0,i}$ on which $x_{0,i}$ and x_i are different, and $l_{0,i} = x_i \cap x_{0,i}$ be the part of $x_{0,i}$ on which $x_{0,i}$ and x_i are the same. Therefore, $x_{0,i} = z_{0,i} \cup l_{0,i}$.

Definition 9 (Tightening the Upper Bounds) *Given a network f , a finite test dataset \mathbf{T}_0 with their upper bounds \mathbf{T} , and a distance metric $\|\cdot\|_D$, the tightening problem is an optimisation problem:*

$$\begin{aligned} & \min_{\mathbf{L}_1} \|\mathbf{L}_0 - \mathbf{L}_1\|_D \\ & \text{s.t. } cl(f, z_{0,i} \cup l_{1,i}) \neq cl(f, z_{0,i} \cup l_{0,i}) \quad \text{for } i = 1, \dots, |\mathbf{L}_0| \end{aligned} \quad (18)$$

where $\mathbf{L}_0 = (l_{0,i})_{i=1 \dots |\mathbf{T}_0|}$, $\mathbf{L}_1 = (l_{1,i})_{i=1 \dots |\mathbf{L}_0|}$, $l_{1,i}, l_{0,i} \in [0, 1]^{|\mathbf{L}_0|}$ have the same shape.

To solve this optimisation problem, we can re-use the tensor-based algorithm for computing lower bounds with minor modifications to the DNN query: Before querying DNN, we apply the \cup operation to merge with $z_{0,i}$, as suggested by Equation (18).

4.3 Convergence

We perform convergence analysis of the proposed method. For simplicity, in the proofs we consider the case of a single input x_0 . The convergence guarantee can be extended easily to a finite set. We first show that grid search can guarantee to find the global optimum given a certain error bound based on the assumption that the neural network satisfies the Lipschitz condition as proved in [19, 31].

Theorem 2 (Guarantee of the global minimum of grid search) *Assume a neural network $f(x) : [0, 1]^n \rightarrow \mathbb{R}^m$ is Lipschitz continuous w.r.t. a norm metric $\|\cdot\|_D$ and its Lipschitz constant is K . By recursively sampling $\Delta = 1/\epsilon$ in each dimension, denoted as $\mathcal{X} = \{x_1, \dots, x_{\Delta^n}\}$, the following relation holds:*

$$\|f_{\text{opt}}(x^*) - \min_{x \in \mathcal{X}} f(x)\|_D \leq K \cdot \|\frac{\epsilon}{2} \mathbf{I}_n\|_D$$

where $f_{\text{opt}}(x^*)$ represents the global minimum value, $\min_{x \in \mathcal{X}} f(x)$ denotes the minimum value returned by grid search, and $\mathbf{I}_n \in \mathbb{R}^{n \times n}$ is an all-ones matrix.

Proof 1 *Based on the Lipschitz continuity assumption of f , we have*

$$\|f(x_1) - f(x_2)\|_D \leq K \cdot \|x_1 - x_2\|_D$$

The ϵ grid search guarantees $\forall \tilde{x} \in [0, 1]^n, \exists x \in \mathcal{X}$ such that $\|x^* - x\|_D \leq \|\frac{\epsilon}{2} \mathbf{I}_n\|_D$, denoted as $\mathcal{X}(\tilde{x})$. Thus the theorem holds as we can always find $\mathcal{X}(x^*)$ from the sampled set \mathcal{X} for the global minimum x^* .

As shown in Sec. 4.2, in each iteration, we apply the grid search to verify the safety of the DNNs (meaning that we preclude adversarial examples) given a lower bound. In combination with Theorem 2, we arrive at the following, which shows the safety guarantee for the lower bounds.

Theorem 3 (Guarantee for Lower Bounds) *Let f denote a DNN and let $x_0 \in [0, 1]^n$ be an input. If our method generates a lower bound $l(f, x_0)$, then $cl(f, x) = cl(f, x_0)$ for all x such that $\|x - x_0\|_0 \leq l(f, x_0)$. I.e., f is guaranteed to be safe for any pixel perturbations with at most $l(f, x_0)$ pixels.*

Theorem 3 (proof in Appendix A.2) shows that the lower bounds generated by our algorithm are the lower bounds of $d_m(f, x_0, \|\cdot\|_D)$. We gradually increase $t = l(f, x_0)$ and re-run the lower bound generation algorithm. Because the number of dimensions of an input is finite, the distance to an adversarial example is also finite. Therefore, the lower bound generation algorithm converges eventually.

Theorem 4 (Guarantee for Upper Bounds) *Let f denote a DNN and $x_0 \in [0, 1]^n$ denote an input. Let $u_i(f, x_0)$ be an upper bound generated by our algorithm for any $i > 0$. Then we have $u_{i+1}(f, x_0) \leq u_i(f, x_0)$ for all $i > 0$, and $\lim_{i \rightarrow \infty} u_i(f, x_0) = d_m(f, x_0, \|\cdot\|_D)$.*

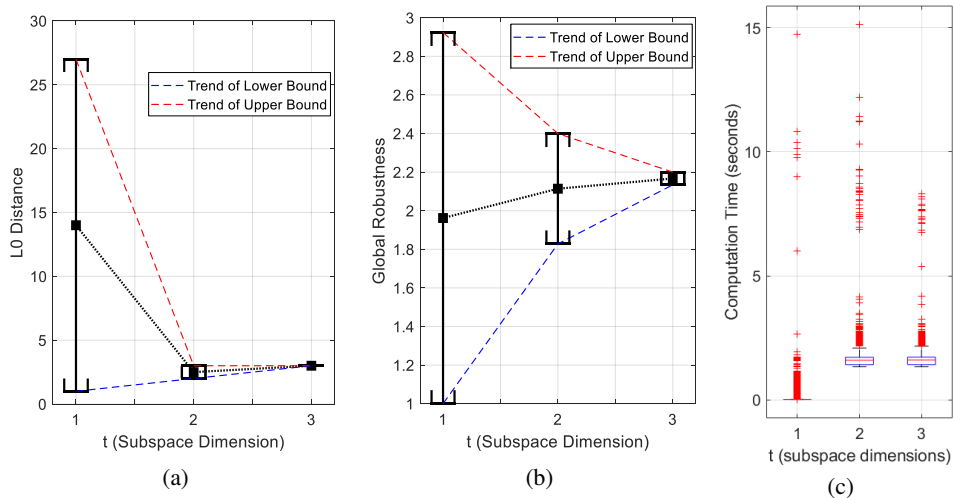


Fig. 1: (a) Convergence of lower bound, upper bound, and estimation of d_m for one image; (b) Convergence of lower bound, upper bound, and estimation of global robustness; (c) Boxplots of the computational time for $t \in \{1, 2, 3\}$

The three key ingredients to show that the upper bounds decrease monotonically are: *i*) the complete subspaces generated at $t = i$ are always included in the complete subspaces at $t = i + 1$; *ii*) the pixel perturbation from a subspace with higher priority always results in a larger confidence decrease than those with lower priority; and *iii*) the tightening strategy is able to exclude the redundant pixel perturbations. The details of the proof for Theorem 4 are in Appendix A.3. Finally, we can show that the radius of $[l_i, u_i]$ will converge to 0 deterministically (see Appendix A.4).

5 Experimental Results

We report experimental evidence for the utility of our algorithm. Some experiments require simple modifications of the optimisation problem given in Definition 3, e.g., small changes to the constraints. No significant modification to our algorithm is needed process to these variants. In this section, we use five case studies to demonstrate the broad applicability of our tool³.

5.1 Case Study One: Convergence Analysis and Global Robustness Evaluation

We study the convergence and running time of our anytime global robustness evaluation algorithm on several DNNs in terms of the L_0 -norm. To the best of our knowledge, no baseline method exists for this case study. The L_0 -norm based algorithms, which we compare against in Section 5.2, cannot perform robustness evaluation based on both lower and upper bounds with provable guarantees.

We train two DNNs on the MNIST dataset, with DNN-0 being trained on the original images of size 28×28 and sDNN on images resized into 14×14 . The model structures are

³ The Case Study Four and Case Study Five are available in the Appendix

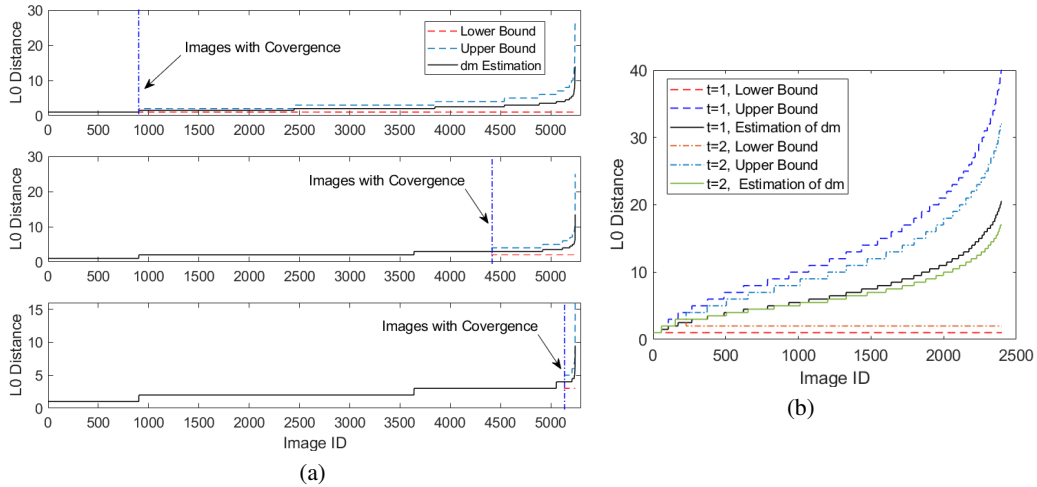


Fig. 2: (a) sDNN: Upper bounds, lower bounds, and estimations of d_m for all sampled images for $t \in \{1, 2, 3\}$ ordered from the top to bottom. (b) DNN-0: Upper bounds, lower bounds, and estimations of d_m for all sampled input images for $t \in \{1, 2\}$

given in Appendix F. For DNN-0, we work with a set of 2,400 images randomly sampled from the dataset, and for sDNN, we work with a set of 5,300 images.

sDNN: Speed of Convergence and Robustness Evaluation Fig. 1 (a) illustrates the speed of convergence of lower and upper bounds as well as the estimate for d_m (i.e., the maximum safe radius) for an image with a large initial upper bound at L_0 distance 27. This image is chosen to demonstrate the *worst case* for our approach. Working with a single image (i.e., local robustness) is the special case of our optimisation problem where $|T| = 1$. We observe that, when transitioning from $t = 1$ to $t = 2$, the uncertainty radius $U_r(l_t, u_t)$ of d_m is significantly reduced from 26 to 1, which demonstrates the effectiveness of our upper bound algorithm. Fig. 1 (b) illustrates the speed of convergence of the global robustness evaluation on the testing dataset: Our method obtains tight upper and lower bounds efficiently and converges quickly. Notably, we have $U_c(l_t, u_t) = 1.97$ at $t = 1$; the final global robustness is 2.1, and thus, the relative error of the global robustness at $t = 1$ is less than 7%. The estimate at $t = 1$ can be obtained in polynomial time, and thus, our experimental results suggest that our approach provides a good approximation for this challenging NP-hard problem with reasonable error at very low computational cost. Fig. 1 (c) gives the boxplots of the computational time required for individual iterations (i.e., subspace dimensions t). We remark that at $t = 1$ it takes less than 0.1 s to process one image, which suggests that the algorithm has potential for real-time applications.

In Fig. 2 (a), we plot the upper and lower bounds as well as the estimate for d_m for all images in the testing dataset. The images are ordered using their upper bounds at $t = 1$. The dashed blue line indicates that all images left of this line have converged. The charts show a clear overall trend: our algorithm converges for most images with after a very small number of iterations.

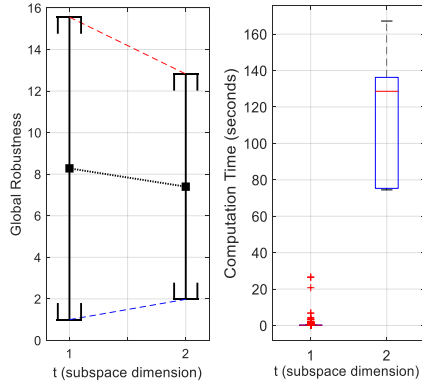


Fig. 3: Robustness evaluation of DNN-0 for $t \in \{1, 2\}$ and box-plots of computation time

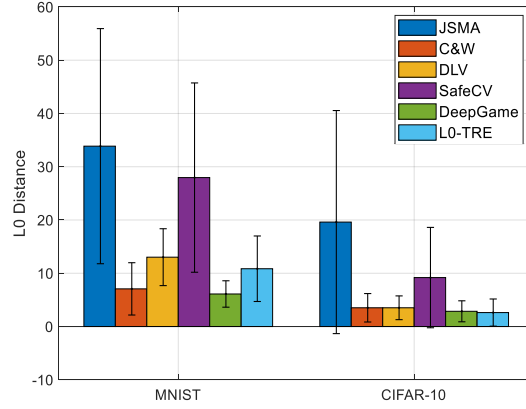


Fig. 4: Means and standard deviations of the adversarial L_0 distance

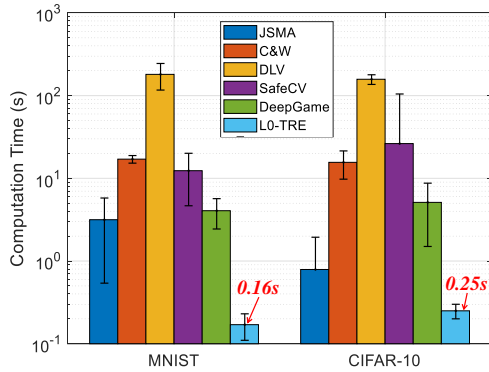


Fig. 5: Means and standard deviations of computational time of all methods

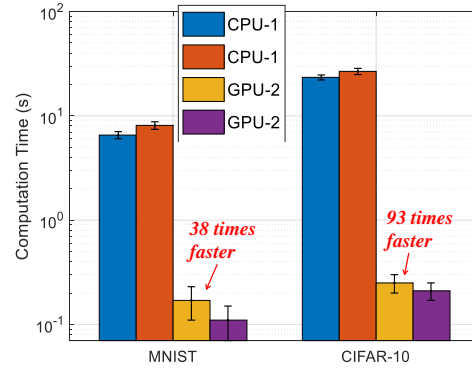


Fig. 6: Means and standard deviations of computational time in CPU and GPU for 1,000 MNIST and CIFAR-10 images

DNN-0: Global Robustness Evaluation Fig. 2 (b) illustrates the overall convergence trends for all 2,400 images for our large DNN. We observe that even for a DNN with tens of thousands of hidden neurons, L0-TRE achieves tight estimates for d_m for most images. Fig. 3 gives the results of anytime global robustness evaluation at $t = 1$ and $t = 2$ for DNN-0. The results show the feasibility and efficiency of our approach for anytime global robustness evaluation of safety-critical systems. Fig. 12 in Appendix F features a selection of the ground-truth adversarial images⁴ returned by our upper bound algorithm.

5.2 Case Study Two: L_0 Attacks

While the generation of attacks is not the primary goal of our method, we observe that our upper bound generation method is highly competitive with state-of-the-art methods for the

⁴ Ground-true adversarial images mean images that are at the boundary of a safe norm ball, which is first proposed in [1].

Table 1: Neuron coverage achieved by L0-TRE, DeepConcolic and DeepXplore

	L0-TRE (%)	DeepConcolic [28] (%)	DeepXplore [20] (%)		
			light	occlusion	blackout
MNIST	98.95	97.60	80.77	82.68	81.61
CIFAR-10	98.63	84.98	77.56	81.48	83.25

computation of adversarial images. We train MNIST and CIFAR-10 DNNs and compare with JSMA [18], C&W [2], DLV [8], SafeCV [31] and DeepGame [32], on 1,000 testing images. Details of the experimental settings are given in Appendix G.

Adversarial L_0 Distance Fig. 4 depicts the average and standard deviations of L_0 distances of the adversarial images produced by the five methods. A smaller L_0 distance indicates an adversarial example closer to the original image. For MNIST, the performance of our method is better than JSMA, DLV, and SafeCV, and comparable to C&W and DeepGame. For CIFAR-10, the bar-chart reveals that our L0-TRE achieves the smallest L_0 distance (modifying 2.62 pixels on average) among all competitors. For this experiment, we stop at $t = 1$ without performing further iterations.

Computational Cost Fig. 5 (note log-scale) gives runtimes. Our tensor-based parallelisation method delivers extremely efficient attacks. For example, for MNIST, our method is $18\times$, $100\times$, $1050\times$, and $357\times$ faster than JSMA, C&W, DLV, and SafeCV, respectively. Figure 6 shows that the tensor-based parallelisation⁵ significantly improves the computational efficiency in terms of 38 times faster on MNIST DNN and 93 times faster on CIFAR-10 DNN. Appendix G compares some of the adversarial examples found by the five methods. The examples illustrate that the modification of one to three pixels suffices to trigger misclassification even in well-trained neural networks.

5.3 Case Study Three: Test Case Generation for DNNs

A variety of methods to automate testing of DNNs has been proposed recently [20, 27, 28]. The most widely used metric for the exhaustiveness of test suites for DNNs is *neuron coverage* [20]. Neuron coverage quantifies the percentage of hidden neurons in the network that are activated at least once. We use ne to range over hidden neurons, and $V(ne, x)$ to denote the activation value of ne for test input x . Then $V(ne, x) > 0$ implies that ne is covered by the test input x .

The application of our algorithm to coverage-driven test case generation is straight forward; it only requires a minor modification to the optimisation problem in Definition 3. Given any neuron ne that is not activated by the test suite T_0 , we find the input with the smallest distance to any input in T_0 that activates ne . We replace the constraint $cl(f, x_i) \neq$

⁵ *CPU-1*: Tensorflow (Python) on i5-4690S CPU; *GPU-1*: Tensorflow (Python) with parallelisation on NVIDIA GTX TITAN GPU. *CPU-2*: Deep Learning Toolbox (Matlab2018b) on i7-7700HQ CPU; *GPU-2*: Deep Learning Toolbox (Matlab2018b) with parallelisation on NVIDIA GTX-1050Ti GPU.



Fig. 7: Some adversarial examples found by our tool L0-TRE while generating test cases for high neuron coverage on MNIST and CIFAR-10 DNNs

$cl(f, x_{0,i})$ in Equation (4) with

$$V(ne, x_i) \leq 0 \wedge V(ne, x_{0,i}) > 0. \quad (19)$$

The optimisation problem now searches for new inputs that activate the neuron ne , and the objective is to minimise the distance from the current set of test inputs T_0 .

We compare our tool L0-TRE with other state-of-the-art test case generation methods, including DeepConcolic⁶ [28] and DeepXplore [20]. All results are averaged over 10 runs or more. Table 1 gives the neuron coverage obtained by the three tools. We observe that L0-TRE yields much higher neuron coverage than both DeepConcolic and DeepXplore in any of its three modes of operation (‘light’, ‘occlusion’, and ‘blackout’). Fig. 7 depicts adversarial examples generated due to L_0 norm change by our tool L0-TRE on test case generation. We also observe that a significant portion of the adversarial examples can be found using a relatively small L_0 distance. More experimental results can be found in Appendix H. Overall, our tool L0-TRE offers an efficient approach to coverage-driven testing on DNNs.

Moreover, our tool can be used to guide the design of robust DNN architectures, as shown in Case Study Four (see Appendix D). In Case Study Five, we show that L0-TRE can also generate saliency map for model interpretability and is capable of evaluating local robustness for large-scale, state-of-the-art ImageNet DNN models including VGG-16/19, ResNet-50/101 and AlexNet (see Appendix E).

6 Related Work

6.1 Generation of Adversarial Examples

Existing algorithms compute an upper bound of the maximum safety radius. However, they cannot guarantee to reach the maximum safety radius, while our method is able to produce both lower and upper bounds that provably converge to the maximum safety radius. Most existing algorithms first compute a gradient (either a cost gradient or a forward gradient) and then perturb the input in different ways along the most promising direction on that gradient. *FGSM* (Fast Gradient Sign Method) [5] is for the L_∞ norm. It computes the gradient $\nabla_x J(\theta, x, f(x))$. *JSMa* (Jacobian Saliency Map based Attack) [18] is for the L_0 norm. It calculates the Jacobian matrix of the output of a DNN (in the logit layer) with respect to

⁶ Our optimisation algorithm has been also adopted in the testing tool *DeepConcolic*, see <https://github.com/TrustAI/DeepConcolic>

the input. Then it iteratively modifies one or two pixels until a misclassification occurs. The *C&W Attack* (Carlini and Wagner) [2] works for the L_0 , L_2 and L_∞ norms. It formulates the search for an adversarial example as an image distance minimisation problem. The basic idea is to introduce a new optimisation variable to avoid box constraints (image pixels need to lie within $[0, 1]$). *DeepFool* [16] works for the L_2 norm. It iteratively linearises the network around the input x and moves across the boundary by a minimal step until reaching a misclassification. *VAT* (Visual Adversarial Training) [15] defines a KL-divergence at an input based on the model’s robustness to the local perturbation of the input, and then perturbs the input according to this KL-divergence. We focus on the L_0 norm. We have shown experimentally that for this norm, our approach dominates all existing approaches. We obtain tighter upper bounds at lower computational cost.

6.2 Safety Verification and Reachability Analysis

The approaches aim to not only find an upper bound but also provide guarantees on the obtained bound. There are two ways of achieving safety verification for DNNs. The first is to reduce the problem to a constraint solving problem. Notable works include, e.g., [9, 21]. However, they can only work with small networks that have hundreds of hidden neurons. The second is to discretise the vector spaces of the input or hidden layers, and then apply exhaustive search algorithms or Monte-Carlo tree search algorithm on the discretised spaces. The guarantees are achieved by establishing local assumptions such as minimality of manipulations in [8] and minimum confidence gap for Lipschitz networks in [31, 32]. Moreover, [12] considers determining if an output value of a DNN is reachable from a given input subspace, and reduces the problem to a MILP problem; and [3] considers the range of output values from a given input subspace. Both approaches can only work with small networks. We also mention [19], which computes a lower bound of local robustness for the L_2 norm by propagating relations between layers backward from the output. It is incompatible with ours because of the different distance metrics. The bound is loose and cannot be improved (i.e., no convergence). Recently, some researchers use abstract interpretation to verify the correctness of DNNs [4, 14]. Its basic idea is to use abstract domains (represented as e.g., boxes, zonotopes, polyhedra) to over-approximate the computation of a set of inputs. In recent work [6] the input vector space is partitioned using clustering and then the method of [9] is used to check the individual partitions. DeepGO [22, 23] shows that most known layers of DNNs are Lipschitz continuous and presents a verification approach based on global optimisation.

However, none of the verification tools above are workable on L_0 -norm distance in terms of providing the *anytime* and *guaranteed* convergence to the true global robustness. Thus, the proposed tool, L0-TRE, is a supplementary to existing research on safety verification of DNNs.

7 Conclusions

In this paper, to evaluate global robustness of a DNN over a testing dataset, we present an approach to iteratively generate its lower and upper bounds. We show that the bounds are gradually, and strictly, improved and eventually converge to the optimal value. The method is anytime, tensor-based, and offers provable guarantees. We conduct experiments on a set of challenging problems to validate our approach.

References

1. Carlini, N., Katz, G., Barrett, C., Dill, D.L.: Ground-truth adversarial examples. arXiv preprint arXiv:1709.10207 (2017)
2. Carlini, N., Wagner, D.: Towards evaluating the robustness of neural networks. In: Security and Privacy (SP), 2017 IEEE Symposium on. pp. 39–57. IEEE (2017)
3. Dutta, S., Jha, S., Sanakranarayanan, S., Tiwari, A.: Output range analysis for deep neural networks. arXiv preprint arXiv:1709.09130 (2017)
4. Gehr, T., Mirman, M., Drachler-Cohen, D., Tsankov, P., Chaudhuri, S., Vechev, M.T.: AI^2 : Safety and robustness certification of neural networks with abstract interpretation. In: 2018 IEEE Symposium on Security and Privacy (SP) (2018)
5. Goodfellow, I.J., Shlens, J., Szegedy, C.: Explaining and harnessing adversarial examples. arXiv preprint arXiv:1412.6572 (2014)
6. Gopinath, D., Katz, G., Pasareanu, C.S., Barrett, C.: DeepSafe: A data-driven approach for checking adversarial robustness in neural networks. In: Automated Technology for Verification and Analysis (ATVA). LNCS, vol. 11138, pp. 3–19. Springer (2018)
7. He, K., Zhang, X., Ren, S., Sun, J.: Deep residual learning for image recognition. In: Proceedings of the IEEE conference on computer vision and pattern recognition. pp. 770–778 (2016)
8. Huang, X., Kwiatkowska, M., Wang, S., Wu, M.: Safety verification of deep neural networks. In: CAV 2017. pp. 3–29 (2017)
9. Katz, G., Barrett, C., Dill, D., Julian, K., Kochenderfer, M.: Reluplex: An efficient SMT solver for verifying deep neural networks. In: CAV 2017 (2017)
10. Krizhevsky, A., Sutskever, I., Hinton, G.E.: ImageNet classification with deep convolutional neural networks. In: Advances in neural information processing systems. pp. 1097–1105 (2012)
11. Kurakin, A., Goodfellow, I., Bengio, S.: Adversarial examples in the physical world. arXiv preprint arXiv:1607.02533 (2016)
12. Lomuscio, A., Maganti, L.: An approach to reachability analysis for feed-forward relu neural networks. CoRR **abs/1706.07351** (2017), <http://arxiv.org/abs/1706.07351>
13. Lundberg, S., Lee, S.: A unified approach to interpreting model predictions. CoRR **abs/1705.07874** (2017), <http://arxiv.org/abs/1705.07874>
14. Mirman, M., Gehr, T., Vechev, M.: Differentiable abstract interpretation for provably robust neural networks. In: International Conference on Machine Learning. pp. 3575–3583 (2018)
15. Miyato, T., Maeda, S.i., Koyama, M., Nakae, K., Ishii, S.: Distributional smoothing with virtual adversarial training. arXiv preprint arXiv:1507.00677 (2015)
16. Moosavi-Dezfooli, S.M., Fawzi, A., Frossard, P.: DeepFool: a simple and accurate method to fool deep neural networks. In: CVPR 2016. pp. 2574–2582 (2016)
17. Olah, C., Satyanarayan, A., Johnson, I., Carter, S., Schubert, L., Ye, K., Mordvintsev, A.: The building blocks of interpretability. Distill (2018). <https://doi.org/10.23915/distill.00010>, <https://distill.pub/2018/building-blocks>
18. Papernot, N., McDaniel, P., Jha, S., Fredrikson, M., Celik, Z.B., Swami, A.: The limitations of deep learning in adversarial settings. In: EuroS&P 2016. pp. 372–387. IEEE (2016)
19. Pec, J., Roels, J., Goossens, B., Saeys, Y.: Lower bounds on the robustness to adversarial perturbations. In: NIPS (2017)
20. Pei, K., Cao, Y., Yang, J., Jana, S.: DeepXplore: Automated whitebox testing of deep learning systems. In: SOSPP 2017. pp. 1–18. ACM (2017)
21. Pulina, L., Tacchella, A.: An abstraction-refinement approach to verification of artificial neural networks. In: CAV 2010. pp. 243–257 (2010)
22. Ruan, W., Huang, X., Kwiatkowska, M.: Reachability analysis of deep neural networks with provable guarantees. The 27th International Joint Conference on Artificial Intelligence (IJCAI’18) (2018)
23. Ruan, W., Huang, X., Kwiatkowska, M.: Reachability analysis of deep neural networks with provable guarantees. arXiv preprint arXiv:1805.02242 (2018)

24. Ruan, W., Wu, M., Sun, Y., Huang, X., Kroening, D., Kwiatkowska, M.: Global robustness evaluation of deep neural networks with provable guarantees for L0 norm. arXiv preprint arXiv:1804.05805 (2018)
25. Simonyan, K., Zisserman, A.: Very deep convolutional networks for large-scale image recognition. arXiv preprint arXiv:1409.1556 (2014)
26. Su, J., Vargas, D.V., Sakurai, K.: One pixel attack for fooling deep neural networks. CoRR **abs/1710.08864** (2017), <http://arxiv.org/abs/1710.08864>
27. Sun, Y., Huang, X., Kroening, D.: Testing deep neural networks. arXiv preprint arXiv:1803.04792 (2018)
28. Sun, Y., Wu, M., Ruan, W., Huang, X., Kwiatkowska, M., Kroening, D.: Concolic testing for deep neural networks. In: Automated Software Engineering (ASE). pp. 109–119. ACM (2018)
29. Szegedy, C., Zaremba, W., Sutskever, I., Bruna, J., Erhan, D., Goodfellow, I., Fergus, R.: Intriguing properties of neural networks. In: In ICLR. Citeseer (2014)
30. Tian, Y., Pei, K., Jana, S., Ray, B.: DeepTest: Automated testing of deep-neural-network-driven autonomous cars. arXiv preprint arXiv:1708.08559 (2017)
31. Wicker, M., Huang, X., Kwiatkowska, M.: Feature-guided black-box safety testing of deep neural networks. In: TACAS 2018 (2018)
32. Wu, M., Wicker, M., Ruan, W., Huang, X., Kwiatkowska, M.: A game-based approximate verification of deep neural networks with provable guarantees. arXiv preprint arXiv:1807.03571 (2018)

A Appendix: Proofs of Theorems

A.1 Proof of NP-hardness

Theorem 5 *Let $f : \mathbb{R}^n \rightarrow \mathbb{R}^m$ be a neural network and its input is normalized into $[0, 1]^n$. When $\|\cdot\|_D$ is the L_0 norm, $d_m(f, x_0, \|\cdot\|_D)$ is NP-hard, and there at least exists a deterministic algorithm that can compute $d_m(f, x_0, \|\cdot\|_D)$ in time complexity $O((1+1/\epsilon)^n)$ for the worst case scenario when the error tolerance for each dimension is $\epsilon > 0$.*

Proof 2 *Here we consider the worst case scenario and use a straight-forward grid search to verify the time complexity needed. In the worst case, the maximum radius of a safe L_0 -norm ball for DNN f is $d_m(f, x_0, \|\cdot\|_D) = n$. A grid search with grid size $\Delta = 1/\epsilon$ starts from $d_{L_0} = 1$ to verify whether d_{L_0} is the radius of maximum safe L_0 -norm ball and would require the following running time in terms of evaluation numbers of the DNN.*

$$\sum_{d_{L_0}=1}^n \binom{n}{d_{L_0}} \Delta^{d_{L_0}} = (1 + 1/\epsilon)^n \quad (20)$$

From the above proof, we get the following remark.

Remark 1 *Computing $d_m(f, x_0, \|\cdot\|_D)$ is more challenging problem for $D = 0$, since it requires a higher computing complexity than $D = 1$ and $D = 2$. Namely, grid search only requires $(1/\epsilon)^n$ evaluations on DNN to estimate $d_m(f, x_0, \|\cdot\|_1)$ or $d_m(f, x_0, \|\cdot\|_2)$ given the same error tolerance ϵ .*

A.2 Proof of Theorem: Guarantee of Lower Bounds

Proof 3 *Our proof proceeds by contradiction. Let $l = l(f, x_0)$. Assume that there is another adversarial example x'_0 such that $t' = \|x'_0 - x_0\|_0 \leq l$ where t' represents the number of perturbed pixels. By the definition of adversarial examples, there exists a subspace $X_k \in \mathbb{R}^{t'}$ such that $cl(f, \mathcal{S}(x_0, t')[:, k]) \neq cl(f, x_0)$. By $t' \leq l$, we can find a subspace $Y_q \in \mathbb{R}^l$ such that $X_k \subset Y_q$. Thus we have $S(Y_q, l) \geq S(X_k, t')$. Moreover, by $S(Y_q, l) \leq S(Y_1, l)$, we have $cl(f, \mathcal{S}(x_0, l)[:, 1]) \neq cl(f, x_0)$ since $cl(f, \mathcal{S}(x_0, l)[:, p]) \neq cl(f, x_0)$. However, this conflicts with $cl(f, \mathcal{S}(x_0, l)[:, 1]) = cl(f, x_0)$, which can be obtained by the algorithm for computing lower bounds in Section 4.2.*

A.3 Proof of Theorem: Guarantee of Upper Bounds

Proof 4 (Monotonic Decrease Property of Upper Bounds) *We use mathematical induction to prove that upper bounds monotonically decrease.*

Base Case $m = 1$: *Based on the algorithm in Upper Bounds of Section 4.2, we assume that, after $m = 1$ subspace perturbations, we find the adversarial example x' such that $cl(f, x') \neq cl(f, x_0)$.*

We know that, at $t = i$, based on the algorithm, we get $S(x_0, i)$ and $\mathcal{S}(x_0, i)$, the ordered subspace sensitivities and their corresponding subspaces. Assume that the ordered subspace list is $\{\phi_1, \phi_2, \dots, \phi_m\}$. Then, from the assumption, we have $cl(f, x(\phi_1)) \neq cl(f, x_0)$ where $x(\phi_1)$ denotes the input of the neural network corresponding to subspace ϕ_1 .

Then, at $t = i + 1$, according to the algorithm, we calculate $S(x_0, i + 1)$ and $\mathcal{S}(x_0, i + 1)$. Similarly, we assume the ordered subspace list is $\{\theta_1, \theta_2, \dots, \theta_n\}$. Thus we can find a subspace θ_q in $\{\theta_1, \theta_2, \dots, \theta_n\}$ such that $\phi_1 \subset \theta_q$. As a result, we know that $S(\phi_1) \leq S(\theta_q)$, thus $cl(f, x(\theta_q)) \neq cl(f, x_0)$. After exhaustive tightening, we can at least find its subset ϕ_1 , since $cl(f, \phi_1) \neq cl(f, x_0)$ still holds after removing the pixels $x = \theta_q - \phi_1$. So we know $\|x(\theta_q) - x_0\|_0 \leq \|x(\phi_1) - x_0\|_0$. However, θ_q will not necessarily be found at $t = i + 1$ in our upper bound algorithm, depending on its location in $\{\theta_1, \theta_2, \dots, \theta_n\}$:

1. If it is in the front position such as $\{\theta_q, \theta_2, \dots, \theta_m\}$, then we know that $\|x(\theta_q) - x_0\|_0 \leq \|x(\phi_1) - x_0\|_0$ based on the above analysis, i.e., $u_i(f, x_0) \geq u_{i+1}(f, x_0)$ holds.

2. If it is in the behind position such as $\{\theta_1, \theta_2, \theta_q, \dots, \theta_m\}$, we know that $S(\theta_1) \geq S(\theta_q) \geq S(\phi_1)$, which means that subspace θ_1 leads to a larger network's confidence decrease than subspace θ_q , thus $\|x(\theta_1) - x_0\|_0 \leq \|x(\theta_q) - x_0\|_0$. We already know $\|x(\theta_q) - x_0\|_0 \leq \|x(\phi_1) - x_0\|_0$, thus $u_i(f, x_0) \geq u_{i+1}(f, x_0)$ also holds.

Inductive Case $m = k$: Assume that at $t = i$, after going through $m = k$ subspace perturbations, i.e., $\Phi_k = \{\phi_1 \cup \phi_2 \cup \dots \cup \phi_k\}$, we find an adversarial example x' and $u_i(f, x_0) \geq u_{i+1}(f, x_0)$ holds. We need to show that after going through $m = k + 1$ subspace perturbations, i.e., $\Phi_{k+1} = \{\phi_1 \cup \phi_2 \cup \dots \cup \phi_k \cup \phi_{k+1}\}$, the relation $u_i(f, x_0) \geq u_{i+1}(f, x_0)$ also holds.

Similarly, at $t = i + 1$, we can find a k subspace set $\Theta_k = \{\theta_{q_1} \cup \theta_{q_2} \cup \dots \cup \theta_{q_k}\}$ such that $\Phi_k \subset \Theta_k$, and we know that $u_{i+1}(f, x_0) = \|x(\Phi_k) - x_0\|_0 \leq \|x(\Theta_k) - x_0\|_0 = u_i(f, x_0)$ holds. Then, for the new subspace ϕ_{k+1} at $t = i$, we can also find $\theta_{q_{k+1}}$ at $t = i + 1$ such that $\phi_{k+1} \subset \theta_{q_{k+1}}$. We get $\Theta_{k+1} = \Theta_k \cup \theta_{q_{k+1}}$. As a result, we still have $\Phi_{k+1} \subset \Theta_{k+1}$, obviously, $cl(x(\Theta_{k+1}), f) \neq cl(x(\Phi_{k+1}), f)$, which means we can definitely find an adversarial example after all perturbations in Θ_{k+1} . After exhaustive tightening process, we can at least find its subset Φ_{k+1} , since $cl(f, x(\Phi_{k+1})) \neq cl(f, x_0)$ still holds after removing those pixels $x = \Theta_k - \phi_k$. So we know $\|x(\Theta_{k+1}) - x_0\|_0 \leq \|x(\Phi_{k+1}) - x_0\|_0$, i.e., $u_i(f, x_0) \geq u_{i+1}(f, x_0)$ holds.

A.4 Proof of Theorem: Uncertainty Radius Convergence to Zero

Proof 5 (Uncertainty Radius Convergence to Zero: $\lim_{t \rightarrow n} U_r(l_i, u_i) = 0$) Based on the definition of L_0 -norm distance (i.e., $0 \leq l_i \leq d_m \leq u_i \leq n$), we know that $t \rightarrow n \implies l_n \rightarrow n \implies U_r(l_i, u_i) = 1/2(u_i - l_i) = n - n = 0$.

B Appendix: The L_0 Norm

We justify on the basis of several aspects that the L_0 norm is worthy of being considered.

Technical Reason The reason why norms other than the L_0 norm are widely used is *mainly technical*: the existing adversarial example generation algorithms [2, 18] proceed by first computing the gradient $\nabla_x J(\theta, x, f(x))$, where $J(\theta, x, f(x))$ is a loss or cost function and θ are the learnable parameters of the network f , and then adapting (in different ways for different algorithms) the input x into x' along the gradient descent direction. To enable this computation, the change to the input x needs to be *continuous and differentiable*. It is not hard to see that, while the L_1 , L_2 and L_∞ norms are continuous and differentiable, the L_0 norm is not. Nevertheless, the L_0 norm is an effective and efficient method to quantify a range of adversarial perturbations and should be studied.

Tolerance of Human Perception to L_0 Norm Recently, [18] demonstrates through in-situ human experiments that the L_0 norm is good at approximating human visual perception. Specifically, 349 human participants were recruited for a study of visual perception on L_0 image distortions, with the result concluding that nearly all participants can correctly recognise L_0 perturbed images when the rate of distortion pixels is less than 5.61% (i.e., 44 pixels for MNIST and 57 pixels for CIFAR-10) and 90% of them can still recognise them when the distortion rate is less than 14.29% (i.e., 112 pixels for MNIST and 146 pixels for CIFAR-10). This experiment essentially demonstrates that human perception is tolerant of perturbations with only a few pixels changed, and shows the necessity of robustness evaluation based on the L_0 norm.

Usefulness of Approaches without Gradient From the security point of view, an attacker to a network may not be able to access its architecture and parameters, to say nothing of the gradient $\nabla_x J(\theta, x, f(x))$. Therefore, to evaluate the robustness of a network, we need to consider *black-box* attackers, which can only query the network for classification. For a black-box attacker, an attack (or a perturbation) based on the L_0 norm is to change several pixels, which is arguably easier to initiate than attacks based on other norms, which often require modifications to nearly all the pixels.

Effectiveness of Pixel-based Perturbations Perturbations by minimising the number of pixels to be changed have been shown to be effective. For example, [26, 31] show that manipulating a single pixel is sufficient for the classification to be changed for several networks trained on the CIFAR10 dataset and the Nexar traffic light challenge. Our approach can beat the state-of-the-art pixel based perturbation algorithms by finding tighter upper bounds to the maximum safety radius. As far as we know, this is the first work on finding lower bounds to the maximum safety radius.

C Appendix: Discussion of Application Scenarios

We now summarise possible application scenarios for the method proposed in this paper.

Safety Verification Safety verification [8] is to determine, for a given network f , an input x_0 , a distance metric $\|\cdot\|_D$, and a number d , whether the norm ball $X(f, x_0, \|\cdot\|_D, d)$ is safe. Our approach will compute a sequence of lower bounds $\mathcal{L}(x_0)$ and upper bounds $\mathcal{U}(x_0)$ for the maximum safe radius $d_m(x_0)$. For every round $i > 0$, we can claim one of the following cases:

- the norm ball $X(f, x_0, \|\cdot\|_D, d)$ is safe when $d \leq \mathcal{L}(x_0)_i$
- the norm ball $X(f, x_0, \|\cdot\|_D, d)$ is unsafe when $d \geq \mathcal{U}(x_0)_i$
- the safety of $X(f, x_0, \|\cdot\|_D, d)$ is unknown when $\mathcal{L}(x_0)_i < d < \mathcal{U}(x_0)_i$.

As a byproduct, our method can return at least one adversarial image for the second case.

Competitive L_0 Attack We have shown that the upper bounds in $\mathcal{U}(x_0)$ are monotonically decreasing. As a result, the generation of upper bounds can serve as a competitive L_0 attack method.

Global Robustness Evaluation Our method can have an asymptotic convergence to the true global robustness with provable guarantees. As a result, for two neural networks f_1 and f_2 that are trained for the same task (e.g., MNIST, CIFAR-10 or ImageNet) but with different parameters or architectures (e.g., different layer types, layer numbers or hidden neuron numbers), if $R(f_1, \|\cdot\|_0) > R(f_2, \|\cdot\|_0)$ then we can claim that network f_1 is more robust than f_2 in terms of its resistance to L_0 -norm adversarial attacks.

Test Case Generation Recently software coverage testing techniques have been applied to DNNs and several test criteria have been proposed, see e.g., [20, 30]. Each criterion defines a set of requirements that have to be tested for a DNN. Given a test suite, the coverage level of the set of requirements indicates the adequacy level for testing the DNN. The technique in this paper can be conveniently used for coverage-based testing of DNNs.

Real-time Robustness Evaluation By replacing the exhaustive search in the algorithm with random sampling and formulating the subspace as a high-dimensional tensor (to enable parallel computation with GPUs), our method becomes *real-time* (e.g., for a MNIST network, it takes around 0.1s to generate an adversarial example). A real-time evaluation can be useful for major safety-critical applications, including self-driving cars, robotic navigation, etc.. Moreover, our method can display in real-time a *saliency map*, visualizing how classification decisions of the network are influenced by pixel-level sensitivities.

D Appendix: Case Study Four: Guiding the Design of Robust DNN Architectures

In this case study, we show how to use our tool L0-TRE for guiding the design of robust DNN architectures.

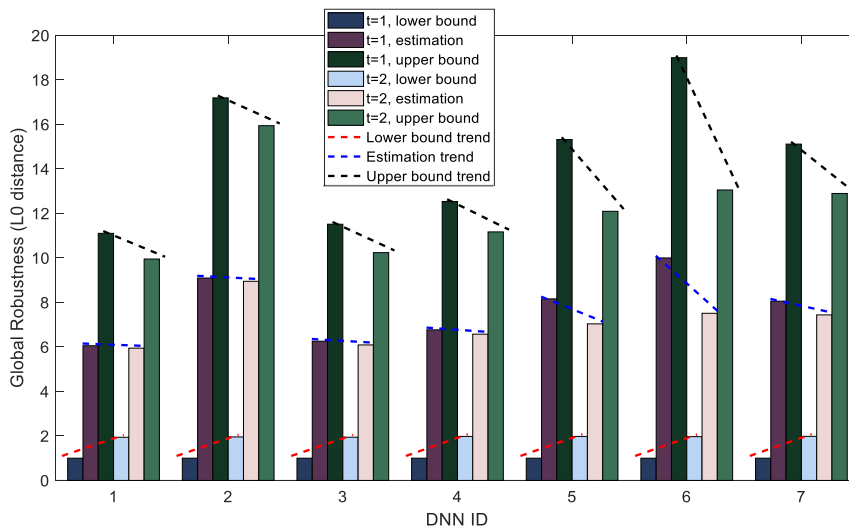


Fig. 8: Lower bounds, upper bounds, and global robustness estimations for $t \in \{1, 2\}$ for seven DNN models

We trained seven DNNs, named DNN- i for $i \in \{1, \dots, 7\}$, on the MNIST dataset using the same hardware and software platform and identical training parameters. The DNNs differ in their architecture, i.e., the number of layers and the types of the layers. The architecture matters: while all DNNs achieve 100% accuracy during training, we observe accuracy down to 97.75% on the testing dataset. Details of the models are in Appendix I. We aim to identify architectural choices that affect robustness.

Fig. 8 gives the estimates for global robustness, and their upper and lower bounds at $t = 1$ and $t = 2$ for all seven DNNs. Fig. 9 illustrates the means and standard deviations of the d_m estimates and the uncertainty radius for all 1,000 sampled testing images. And we also find that, the local robustness (i.e., robustness evaluated on a single image) of a network is coincident with its global robustness, so is the uncertainty radius.

We observe the following: *i*) number of layers: a very deep DNN (i.e., too many layers relative to the size of the training dataset) is less robust, such as DNN-7; *ii*) convolutional layers: DNNs with an excessive number of convolutional layers are less robust, e.g., compared with DNN-5, DNN-6 has an additional convolutional layer, but is significantly less robust; *iii*) batch-normalisation layers: adding a batch-normalisation layer may improve robustness, e.g., DNN-3 is more robust than DNN-2.

We remark that testing accuracy is not a good proxy for robustness: a DNN with higher testing accuracy is not necessarily more robust, e.g., DNN-1 and DNN-3 are more robust

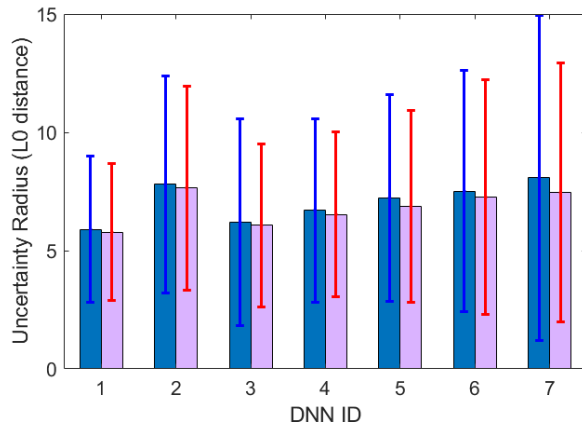


Fig. 9: The means and standard derivations of d_m uncertainty radiuses for 1,000 tested images at $t = 1, 2$.

than DNN-6 and DNN-7, which have higher testing accuracies. DNNs may require a balance between robustness and their ability to generalise (proxied by testing accuracy). DNN-4 is a good example, among our limited set.

In summary, our tool L0-TRE can be used to choose what kind of layers should be added into a deep learning model for a safety-critical system, or given two neural networks with similar testing accuracies, which one should be chose, or finding a balanced model between robustness and performance.

E Appendix: Case Study Five: Saliency Map and Local Robustness Evaluation for Large-scale ImageNet DNN Models

E.1 Local Robustness Evaluation for ImageNet Models

We apply our method to five state-of-the-art ImageNet DNN models, including AlexNet (8 layers), VGG-16 (16 layers), VGG-19 (19 layers), ResNet50 (50 layers), and ResNet101 (101 layers). We set $t = 1$ and generate the lower/upper bounds and estimates of local robustness for an input image. Fig. 10 gives the local robustness estimates and their bounds for these networks. The adversarial images on the upper boundaries are featured in the top row of Fig. 11. For AlexNet, on this specific image, L0-TRE is able to find its ground-truth adversarial example (local robustness converges at $L_0 = 2$). We also observe that, for this image, the most robust model is VGG-16 (local robustness = 15) and the most vulnerable one is AlexNet (local robustness = 2). Fig. 10 also reveals that, for similar network structures such as VGG-16 and VGG-19, ResNet50 and ResNet101, a model with deeper layers is less robust to adversarial perturbation. This observation is consistent with our conclusion in Case Study Three.

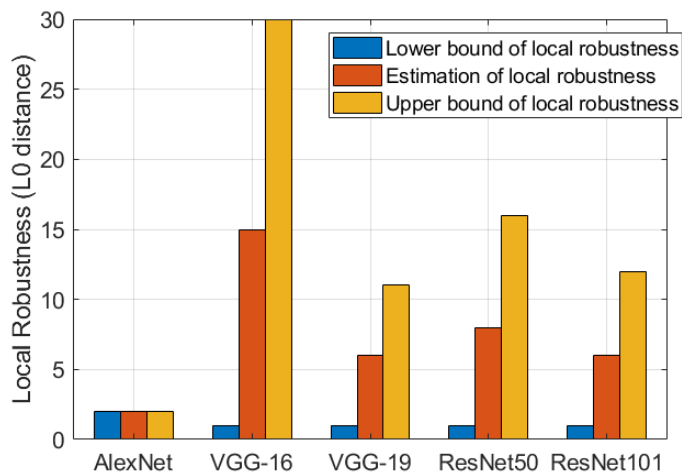


Fig. 10: The upper bound, lower bound and estimation of local robustness for five ImageNet DNNs on a given input image

The method proposed in this paper, just as shown in this case study, provide a possible way to practically evaluate the robustness for large-scale DNN models and such robustness evaluation is with provable bounded guarantees. As a byproduct, our method can also generate saliency map for each input image as shown by the second column of Fig. 11.

E.2 Saliency Map Generation

Model interpretability (or explainability) addresses the problem that the decisions of DNNs are difficult to explain. Recent work, such as [13], calculates the contribution of each input

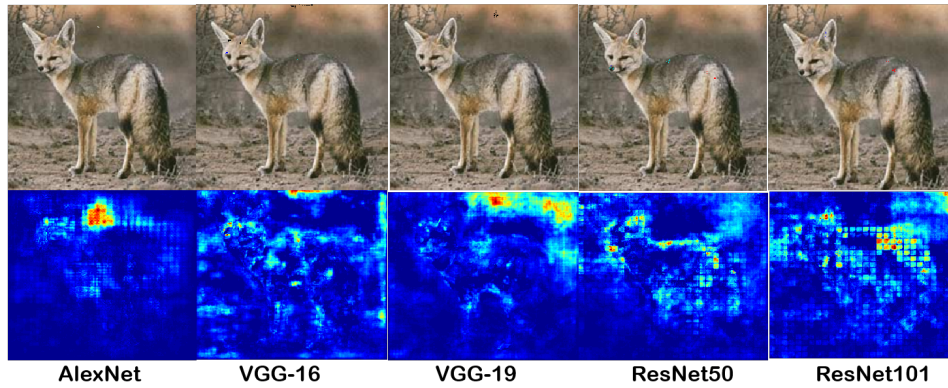


Fig. 11: Adversarial examples on upper boundaries (top) and saliency maps (bottom)

dimension to the output decision. Our computation of subspace sensitivity $S(T, t)$ can be re-used to quantify this contribution for each pixel of an image.

As shown in Fig. 11 (more examples in Appendix J), a brighter area indicates vulnerability to perturbation; it is very easy to see that VGG-16 is the most robust model. We obtain a large bright area for AlexNet, where a minor perturbation can lead to a misclassification. On the contrary, for this image, there are no vulnerable areas for VGG-16. The constraints of the optimisation problem given in Definition 3 can be adapted to generate full saliency maps for the hidden neurons, which have potential as an explanation for the decisions that DNNs make [17]. Moreover, a classic concept in cooperative game theory is to calculate the contribution of the players to their cooperation. Quantifying such contribution values play an important role in game-based safety verification on DNNs such as recent works in [31, 32]. The intermediate result from L0-TRE tool in terms of subspace sensitivity $S(T, t)$, as shown in this case study, is well suitable for this purpose as validated in paper [32].

F Appendix: Experimental Settings for Case Study One

F.1 Model Structures of sDNN

Table 2: sDNN

Layer Type	Size
Input layer	$14 \times 14 \times 1$
Convolution layer	$2 \times 2 \times 8$
Batch-Normalization layer	8 channels
ReLU activation	
Convolution layer	$2 \times 2 \times 16$
Batch-Normalization layer	16 channels
ReLU activation	
Convolution layer	$2 \times 2 \times 32$
Batch-Normalization layer	32 channels
ReLU activation	
Fully Connected	10
softmax + Class output	

F.2 Parameter Settings of sDNN

Model Training Setup

- Hardware: Notebook PC with I7-7700HQ, 16GB RAM, GTX 1050 GPU
- Software: Matlab 2018a, Neural Network Toolbox, Image Processing Toolbox, Parallel Computing Toolbox
- Parameter Optimization Settings: SGDM, Max Epochs = 20, Mini-Batch Size = 128
- Training Dataset: MNIST training dataset with 50,000 images
- Training Accuracy: 99.5%
- Testing Dataset: MNIST testing dataset with 10,000 images
- Testing Accuracy: 98.73%

Algorithm Setup

- $\epsilon = 0.25$
- Maximum $t = 3$
- Tested Images: 5,300 images sampled from MNIST testing dataset

F.3 Model Structures of DNN-0

F.4 Parameter Settings of DNN-0

Model Training Setup

- Hardware: Notebook PC with I7-7700HQ, 16GB RAM, GTX 1050 GPU

Table 3: DNN-0

Layer Type	Size
Input layer	$28 \times 28 \times 1$
Convolution layer	$3 \times 3 \times 32$
ReLU activation	
Convolution layer	$3 \times 3 \times 64$
ReLU activation	
Maxpooling layer	2×2
Dropout layer	0.25
Fully Connected layer	128
ReLU activation	
Dropout layer	0.5
Fully Connected layer	10
Softmax + Class output	

- Software: Matlab 2018a, Neural Network Toolbox, Image Processing Toolbox, Parallel Computing Toolbox
- Parameter Optimization Settings: SGDM, Max Epochs = 30, Mini-Batch Size = 128
- Training Dataset: MNIST training dataset with 50,000 images
- Training Accuracy: 100%
- Testing Dataset: MNIST testing dataset with 10,000 images
- Testing Accuracy: 99.16%

Algorithm Setup

- $\epsilon = 0.25$
- Maximum $t = 2$
- Tested Images: 2,400 images sampled from MNIST testing dataset

F.5 Ground-Truth Adversarial Images

Fig. 12 displays some adversarial images returned by our upper bound algorithm.



Fig. 12: Ground truth adversarial examples when converging to d_m . For each digital image, from the left to right, the first is original image, the second is the adversarial image returned at $t = 1$, and the third is the adversarial example at the boundary of a safe norm ball, namely the ground-truth adversarial examples [1].



Fig. 13: Ground-truth adversarial examples (right column) generated by L0-TRE at $t = 1$, and the saliency maps of the original images (left column).

G Appendix: Experimental Settings for Case Study Two

G.1 Model Structures for L_0 Attack

The architectures for the MNIST and CIFAR-10 models used in L_0 attack are illustrated in Table 4.

Table 4: Model architectures for the MNIST and CIFAR-10 models.

Layer Type	MNIST	CIFAR-10
Convolution + ReLU	$3 \times 3 \times 32$	$3 \times 3 \times 64$
Convolution + ReLU	$3 \times 3 \times 32$	$3 \times 3 \times 64$
Max Pooling	2×2	2×2
Convolution + ReLU	$3 \times 3 \times 64$	$3 \times 3 \times 128$
Convolution + ReLU	$3 \times 3 \times 64$	$3 \times 3 \times 128$
Max Pooling	2×2	2×2
Flatten		
Fully Connected + ReLU	200	256
Dropout	0.5	0.5
Fully Connected + ReLU	200	256
Fully Connected	10	10

G.2 Model Training Setups

- Parameter Optimization Option: Batch Size = 128, Epochs = 50, Loss Function = `tf.nn.softmax_cross_entropy_with_logits`, Optimizer = `SGD(lr=0.01, decay=1e-6, momentum=0.9, nesterov=True)`
- Training Accuracy:
 - MNIST (99.99% on 60,000 images)
 - CIFAR-10 (99.83% on 50,000 images)
- Testing Accuracy:
 - MNIST (99.36% on 10,000 images)
 - CIFAR-10 (78.30% on 10,000 images)

G.3 Adversarial Images

Fig. 14 and 15 present a few adversarial examples generated on the MNIST and CIFAR-10 datasets by our approach L_0 -TRE, together with results for four other tools, i.e., C&W, JSMA, DLV, and SafeCV.

G.4 Experimental Setting for Competitive L_0 Attack Comparison

Baseline Methods We choose four well-established baseline methods that can perform state-of-the-art L_0 adversarial attacks. Their code is available on GitHub.

- JSMA⁷: is a targeted attack based on the L_0 -norm, here used so that adversarial examples are misclassified into all classes except the correct one.
- C&W⁸: is a state-of-the-art adversarial attack method, which models the attack problem as an unconstrained optimization problem that is solvable by the Adam optimizer in Tensorflow.
- DLV⁹: is an untargeted DNN verification method based on exhaustive search and Monte Carlo tree search (MCTS).
- SafeCV¹⁰: is a feature-guided black-box safety verification and attack method based on the Scale Invariant Feature Transform (SIFT) for feature extraction, game theory, and MCTS.
- DeepGame¹¹: is a two-player turn-based game framework for the verification of deep neural networks with provable guarantees on L_1 , L_2 and L_∞ -norm distances, but with a slight modification it can be used to perform L_0 -norm adversarial attack.

Dataset We perform comparison on two datasets - MNIST and CIFAR-10. They are standard benchmark datasets for adversarial attack of DNNs, and are widely adopted by all these baseline methods.

- MNIST dataset¹²: is an image dataset of handwritten digits, which contains a training set of 60,000 examples and a test set of 10,000 examples. The digits have been size-normalized and centered in a fixed-size image.
- CIFAR-10 dataset¹³: is an image dataset of 10 mutually exclusive classes, i.e., ‘airplane’, ‘automobile’, ‘bird’, ‘cat’, ‘deer’, ‘dog’, ‘frog’, ‘horse’, ‘ship’, ‘truck’. It consists of 60,000 32x32 colour images - 50,000 for training, and 10,000 for testing.

Platforms

- Hardware Platform:
 - NVIDIA GeForce GTX TITAN Black
 - Intel(R) Core(TM) i5-4690S CPU @ 3.20GHz × 4
- Software Platform:
 - Ubuntu 14.04.3 LTS
 - Fedora 26 (64-bit)
 - Anaconda, PyCharm

G.5 Algorithm Settings

MNIST and CIFAR-10 use the same settings, unless separately specified.

⁷ https://github.com/tensorflow/cleverhans/blob/master/cleverhans_tutorials/mnist_tutorial_jsma.py

⁸ https://github.com/carlini/nn_robust_attacks

⁹ <https://github.com/TrustAI/DLV>

¹⁰ <https://github.com/matthewwicker/SafeCV>

¹¹ <https://github.com/TrustAI/DeepGame>

¹² <http://yann.lecun.com/exdb/mnist/>

¹³ <https://www.cs.toronto.edu/~kriz/cifar.html>

- JSMA:
 - bounds = (0, 1)
 - predicts = 'logits'
- C&W:
 - targeted = False
 - learning_rate = 0.1
 - max_iteration = 100
- DLV:
 - mcts_mode = "sift_twoPlayer"
 - startLayer, maxLayer = -1
 - numOfFeatures = 150
 - featureDims = 1
 - MCTS_level_maximal_time = 30
 - MCTS_all_maximal_time = 120
 - MCTS_multi_samples = 5 (MNIST), 3 (CIFAR-10)
- SafeCV:
 - MANIP = max_manip (MNIST), white_manipulation (CIFAR-10)
 - VISIT_CONSTANT = 1
 - backtracking_constant = 1
 - simulation_cutoff = 100
- DeepGame
 - gameType = 'cooperative'
 - bound = 'ub'
 - algorithm = 'A*'
 - eta = ('L0', 30)
 - tau = 1
- Ours:
 - EPSILON = 0.5
 - L0_UPPER_BOUND = 100

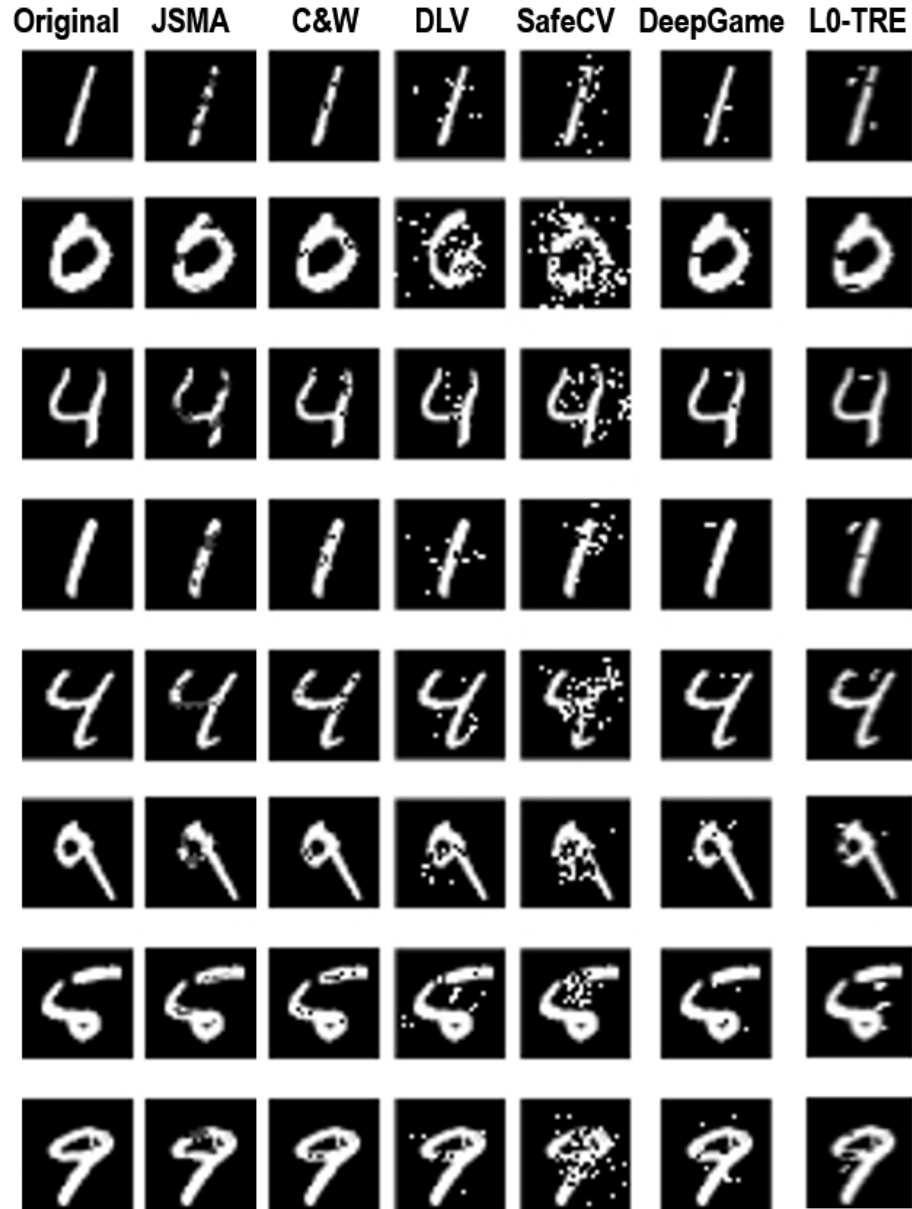


Fig. 14: Adversarial images generated by the L_0 attack methods on the MNIST dataset. From left to right: original image, JSMA, C&W, DLV, SafeCV, DeepGame, and our tool L0-TRE.

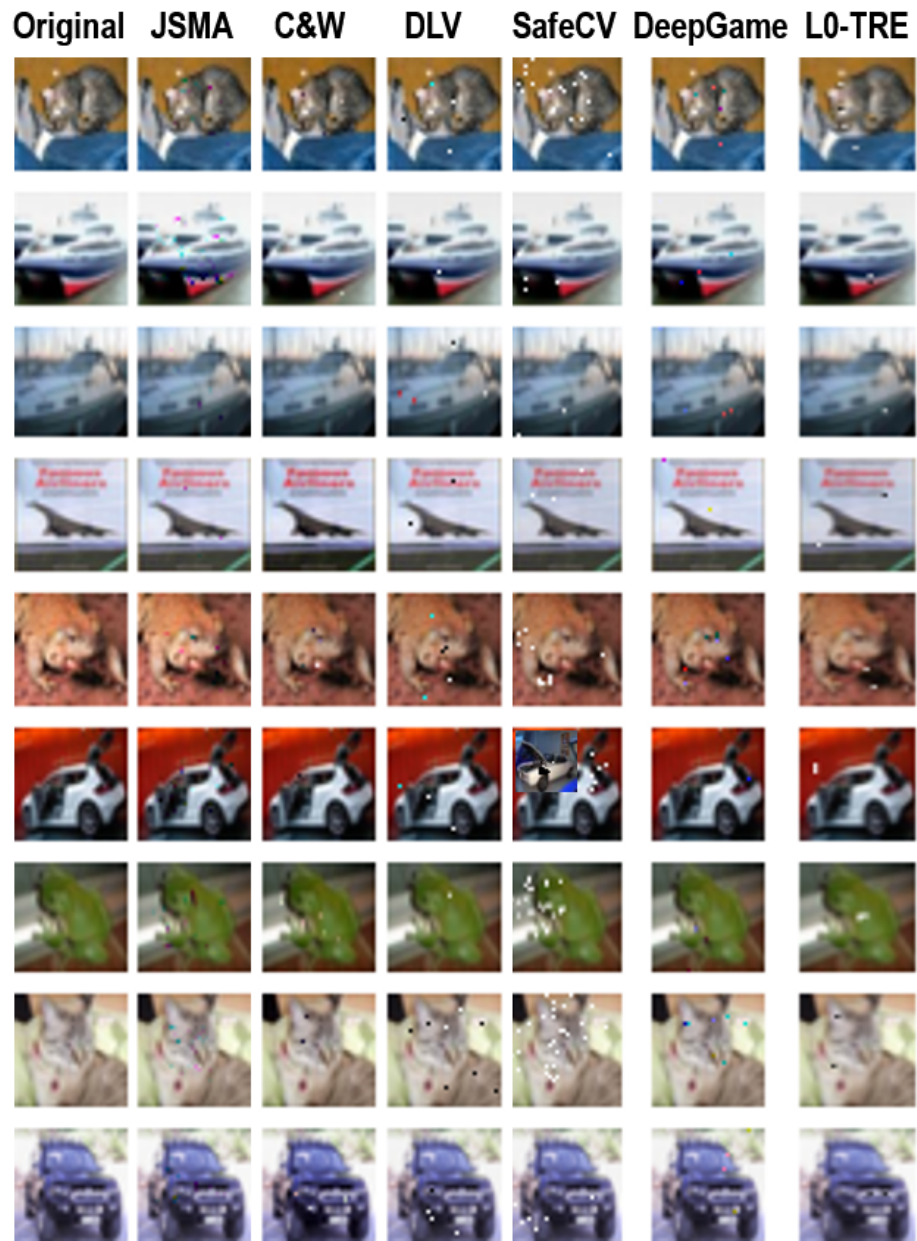
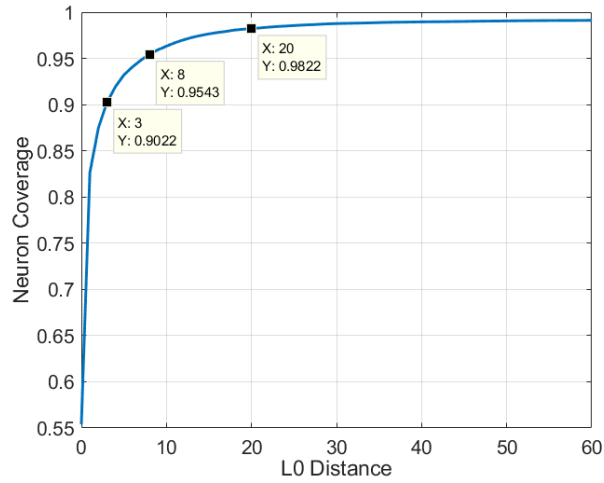


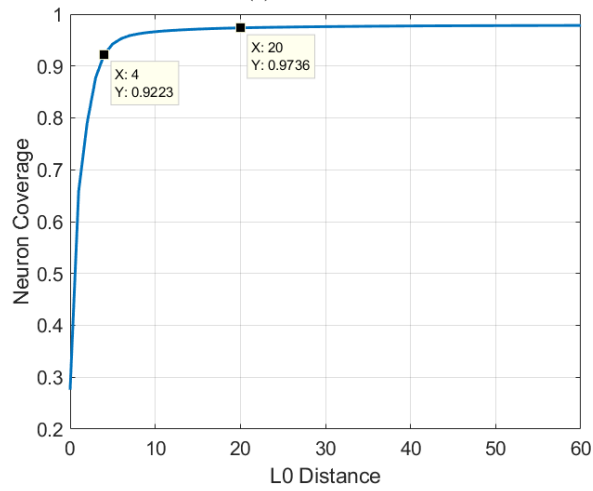
Fig. 15: Adversarial images generated by the L_0 attack methods on the CIFAR-10 dataset. From left to right: original image, JSMA, C&W, DLV, SafeCV, DeepGame, and our tool L0-TRE.

H Appendix: Experimental Settings for Case Study Three

The experimental settings of this case study can be found in Appendix G.



(a) MNIST



(b) CIFAR-10

Fig. 16: Neuron coverage by robustness evaluation on MNIST (a) and CIFAR-10 (b). The horizontal axis measures the L_0 distance of each generated test case with respect to the original input, and the vertical axis records the coverage percentage. We see that it achieves more than %90 neuron coverage by only modifying 3 pixels.

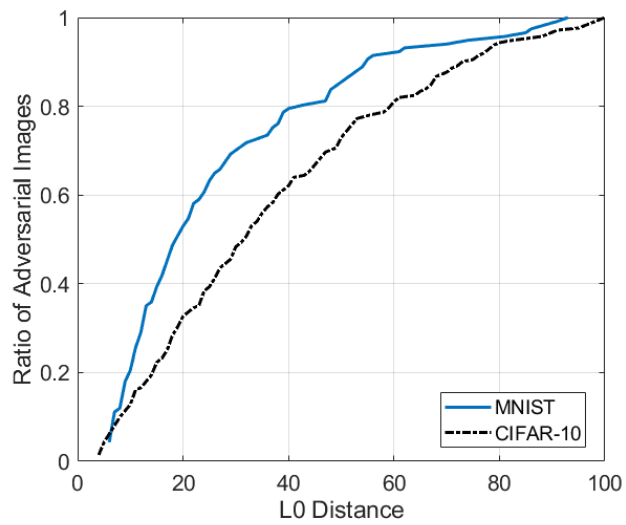


Fig. 17: Neuron coverage: the percentage of adversarial examples within each distance. *It depicts that a significant portion of adversarial examples can be found in the relatively small L_0 distance end of the curve.* More experimental results and applications of applying L0-TRE into DNN testing can be found in GitHub <https://github.com/TrustAI/DeepConcolic>

I Appendix: Experimental Settings for Case Study Four

I.1 Model Training and Algorithm Setup

- Hardware: Notebook PC with I7-7700HQ, 16GB RAM, GTX 1050 GPU
- Software: Matlab 2018a, Neural Network Toolbox, Image Processing Toolbox, Parallel Computing Toolbox
- Parameter Optimization Settings: SGDM, Max Epochs = 30, Mini-Batch Size = 128
- Training Dataset: MNIST training dataset with 50,000 images
- Training Accuracy: All seven models reach 100%
- Testing Dataset: MNIST testing dataset with 10,000 images
- Testing Accuracy: DNN-1 = 97.75%; DNN-2 = 97.95%; DNN-3 = 98.38%; DNN-4 = 99.06%; DNN-5 = 99.16%; DNN-6 = 99.13%; DNN-7 = 99.41%
- L0-TRE Algorithm Setup: $\epsilon = 0.3$, Maximum $t = 2$, Tested Images: 1,000 images sampled from MNIST testing dataset

I.2 Model Structures of DNN-1 to DNN-7

The model structures of DNN-1 to DNN-7 are described in respective tables.

Table 5: DNN-1

Layer Type	Size
Input layer	$28 \times 28 \times 1$
Convolution layer	$3 \times 3 \times 32$
ReLU activation	
Fully Connected layer	10
Softmax + Class output	

Table 6: DNN-2

Layer Type	Size
Input layer	$28 \times 28 \times 1$
Convolution layer	$3 \times 3 \times 32$
ReLU activation	
Convolution layer	$3 \times 3 \times 64$
ReLU activation	
Fully Connected layer	10
Softmax + Class output	

Table 7: DNN-3

Layer Type	Size
Input layer	$28 \times 28 \times 1$
Convolution layer	$3 \times 3 \times 32$
ReLU activation	
Convolution layer	$3 \times 3 \times 64$
Batch-Normalization layer	
ReLU activation	
Fully Connected layer	10
Softmax + Class output	

Table 8: DNN-4

Layer Type	Size
Input layer	$28 \times 28 \times 1$
Convolution layer	$3 \times 3 \times 32$
ReLU activation	
Convolution layer	$3 \times 3 \times 64$
Batch-Normalization layer	
ReLU activation	
Fully Connected layer	128
ReLU activation	
Fully Connected layer	10
Softmax + Class output	

Table 9: DNN-5

Layer Type	Size
Input layer	$28 \times 28 \times 1$
Convolution layer	$3 \times 3 \times 32$
ReLU activation	
Convolution layer	$3 \times 3 \times 64$
Batch-Normalization layer	
ReLU activation	
Dropout layer	0.5
Fully Connected layer	128
ReLU activation	
Fully Connected layer	10
Softmax + Class output	

Table 10: DNN-6

Layer Type	Size
Input layer	$28 \times 28 \times 1$
Convolution layer	$3 \times 3 \times 32$
ReLU activation	
Convolution layer	$3 \times 3 \times 64$
ReLU activation	
Convolution layer	$3 \times 3 \times 128$
Batch-Normalization layer	
ReLU activation	
Dropout layer	0.5
Fully Connected layer	128
ReLU activation	
Fully Connected layer	10
Softmax + Class output	

Table 11: DNN-7

Layer Type	Size
Input layer	$28 \times 28 \times 1$
Convolution layer	$3 \times 3 \times 16$
ReLU activation	
Convolution layer	$3 \times 3 \times 32$
Batch-Normalization layer	
ReLU activation	
Convolution layer	$3 \times 3 \times 64$
Batch-Normalization layer	
ReLU activation	
Convolution layer	$3 \times 3 \times 128$
Batch-Normalization layer	
ReLU activation	
Dropout layer	0.5
Fully Connected layer	256
ReLU activation	
Dropout layer	0.5
Fully Connected layer	10
Softmax + Class output	

J Appendix: Experimental Settings for Case Study Five

J.1 State-of-the-art ImageNet DNN Models

- AlexNet [10] : a convolutional neural network, which was originally designed in the ImageNet Large Scale Visual Recognition Challenge in 2012. The network achieved a top-5 error of 15.3%, more than 10.8 percentage points ahead of the runner up.
- VGG-16 and VGG-19 [25] : were released in 2014 by the Visual Geometry Group at the University of Oxford. This family of architectures achieved second place in the 2014 ImageNet Classification competition, achieving 92.6% top-five accuracy on the ImageNet 2012 competition dataset.
- ResNet50 and ResNet101 [7] : are designed based on residual nets with a depth of 50 and 101 layers. An ensemble of these networks achieved 3.57% testing error on ImageNet and won the 1st place on the ILSVRC 2015 classification task. Their variants also won 1st places on the tasks of ImageNet detection, ImageNet localization, COCO detection, and COCO segmentation.

J.2 Experimental Settings

Platforms

- Hardware: Notebook PC with I7-7700HQ, 16GB RAM, GTX 1050 GPU
- Software: Matlab 2018a, Neural Network Toolbox, Image Processing Toolbox, Parallel Computing Toolbox, and AlexNet, VGG-16, VGG-19, ResNet50 and ResNet101 Pretrained DNN Models

Algorithm Setup

- $\epsilon = 0.3$
- Maximum $t = 1$
- Tested Images: 20 ImageNet images, randomly chosen

J.3 Adversarial Images and Saliency Maps

Fig. 18 gives more examples of adversarial images and saliency maps.

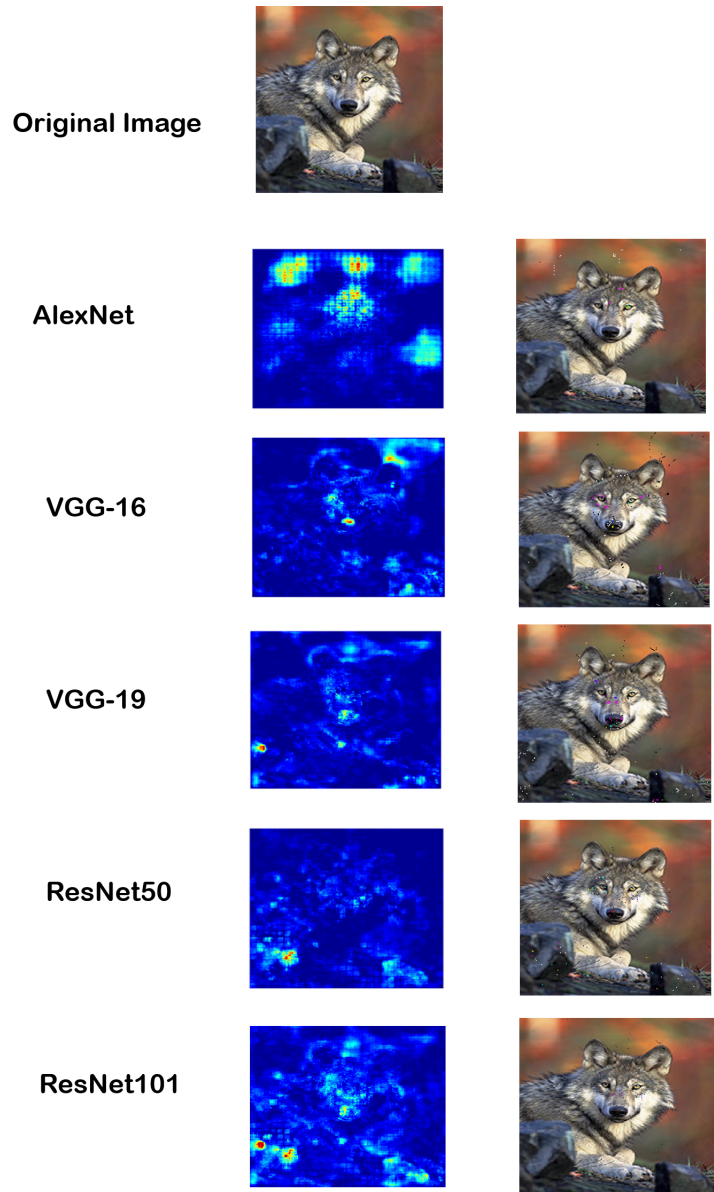


Fig. 18: Adversarial examples on upper boundaries returned by our tool L0-TRE (right column), and saliency maps for each ImageNet DNN model (left column).



Fig. 19: Adversarial examples on upper boundaries (right column) and their saliency maps (left column) for ImageNet AlexNet DNNs. Note that all adversarial images with $L_0 = 1, 2$ are also the ground-truth L_0 -norm adversarial images since their upper bounds and lower bounds local robustness have converged.



Fig. 20: Adversarial examples on upper boundaries (right column) returned by L0-TRE, and their saliency maps (left column) for VGG-16 and VGG-19. The first and second columns are for VGG-16; the third and fourth columns are for VGG-19.